Open access • Posted Content • DOI:10.1101/2020.08.06.230722

Morphologically constrained modeling of spinous inhibition in the somato-sensory cortex — Source link

Olivier Gemin, Pablo Serna, Nora Assendorp, Matteo Fossati ...+3 more authors

Institutions: École Normale Supérieure

Published on: 14 Oct 2020 - bioRxiv (Cold Spring Harbor Laboratory)

Topics: Dendritic spine, Synaptic plasticity and Sensory cortex

Morphologically constrained modeling of spinous inhibition in the somato-sensory cortex

Olivier Gemin[1,2,†], Pablo Serna[1,3,†], Nora Assendorp[1], Matteo Fossati[1,4,5], Philippe Rostaing[1], Antoine Triller[1 *] and Cécile Charrier[1 *]

[1] Institut de Biologie de l'Ecole normale supérieure (IBENS), CNRS, INSERM, PSL Research University, 75005 Paris, France

[2] Present address: Structural and Computational Biology Unit, European Molecular Biology Laboratory, 69117 Heidelberg, Germany

[3] Laboratoire de Physique de l'Ecole Normale Supérieure, ENS, PSL Research University, CNRS, Sorbonne Université, Université Paris-Diderot, Sorbonne Paris Cité, Paris, France 75005

[4] Present address: CNR – Institute of Neuroscience, via Manzoni 56, 20089 Rozzano (MI), Italy

[5] Present address: Humanitas Clinical and Research Center - IRCCS -, via Manzoni 56 20089, Rozzano (MI), Italy

[†]: Contributed equally to this work

*: Corresponding authors

Correspondence to: antoine.triller@ens.psl.eu and cecile.charrier@ens.psl.eu

ABSTRACT

Pyramidal neurons are covered by thousands of dendritic spines receiving excitatory synaptic inputs. The ultrastructure of dendritic spines shapes signal compartmentalization but ultrastructural diversity is rarely taken into account in computational models of synaptic integration. Here, we developed a 3D correlative light-electron microscopy (3D-CLEM) approach allowing the analysis of specific populations of synapses in genetically defined neuronal types in intact brain circuits. We used it to reconstruct segments of basal dendrites of layer 2/3 pyramidal neurons of adult mouse somatosensory cortex and quantify spine ultrastructural diversity. We found that 10% of spines were dually-innervated and 38% of inhibitory synapses localized to spines. Using our morphometric data to constrain a model of synaptic signal compartmentalization, we assessed the impact of spinous versus dendritic shaft inhibition. Our results indicate that spinous inhibition is locally more efficient than shaft inhibition and that it can decouple voltage and calcium signaling, potentially impacting synaptic plasticity.

INTRODUCTION

In the mammalian cortex, the vast majority of excitatory synapses are formed on dendritic spines, small membrane protrusions that decorate the dendrites of pyramidal neurons (PNs) [1–3]. Dendritic spines are composed of a bulbous head connected to the dendritic shaft by a narrow neck [4,5]. They exist in a large variety of shapes and sizes along individual dendrites. Spine head volume can vary between 3 orders of magnitude (0.01-1.5 μm^3), neck length between 0.2 µm and 3 µm, and minimal neck diameter between 20 and 500 nm [6]. Spine heads are typically contacted by an excitatory synaptic input and harbor an excitatory postsynaptic density (ePSD) that contains glutamatergic α-amino-3-hydroxy-5-methyl-4-isoxazolepropionic acid (AMPA) and N-Methyl-D-aspartate (NMDA) neurotransmitter receptors, scaffolding proteins, adhesion molecules and a complex machinery of proteins undertaking the transduction of synaptic signals. The size of the spine head correlates with the size of the ePSD and the strength of synaptic transmission [7–11]. In addition to the

ePSD, spines contain ribosomes, which mediate local protein synthesis, and endosomes, which play a critical role in membrane and receptor trafficking [12,13]. The largest spines often contain a spine apparatus (SA), which contributes to calcium signaling and synaptic plasticity [12,14], and some spines, especially in the upper layers of the cortex, also house an inhibitory postsynaptic specialization [15]. Spine necks are diffusional barriers that biochemically isolate spine heads from their parent dendrite [16–19]. In addition, they can filter the electrical component of synaptic signals and amplify spine head depolarization [20–22] (but see [23–25]). Both spine heads and spine necks are remodeled depending on neuronal activity [9,26,27] and in pathology [28,29]. While the relationship between spine morphology and spine function is widely acknowledged, and although dendritic spines are known to participate in different neural circuits depending on their location in the dendritic tree [30], the extent of synaptic ultrastructural diversity along individual identified dendrites has not been quantified, and the consequences of this variability on signal compartmentalization and dendritic integration remain to be investigated.

Dendritic signaling can be modeled based on anatomical and biophysical parameters [31] using “realistic” multi-compartment models [32]. These models were pioneered by Wilfrid Rall following the seminal works of Hodgkin and Huxley [33,34]. They have provided a powerful theoretical framework for understanding dendritic integration [35], spine function [36], inhibitory signaling [37,38] and electrical compartmentalization in spines [22,39,40]. However, spines and synapses are usually modeled with *ad hoc* or averaged biophysical parameters, which limits the accuracy of the prediction [41]. Modeling the actual behavior of dendritic spines requires an accurate description of their ultrastructural heterogeneity with a cell type and dendritic type resolution. To acquire such data, it is necessary to combine the nanometer resolution of electron microscopy (EM) with an approach that allows the identification of the origin of dendritic spines (i.e. location on the dendrite, type of dendrite and type of neuron) without obscuring the intracellular content. This task is arduous: 1 mm^3 of mouse cortex contains over 50,000 of neurons, each of which establishes approximately 8,000 synaptic connections with neighboring neurons, and these synapses are highly

specific, connecting multiple neuronal subtypes from various brain regions [42–45]. Reconstructing selected dendritic spines and synaptic contacts along dendritic trees requires either enormous volumes of 3D-EM acquisitions using resource-consuming approaches adapted from connectomics [46–49], or combining EM with a lower-scale imaging modality, such as confocal or 2-photon light microscopy (LM), to guide 3D-EM image acquisitions to the region of interest (ROI) [50–52]. While very powerful *in vitro* [50,53,54], correlative light-electron microscopy (CLEM) is difficult to implement in brain tissues [55–57]. New protocols are required to facilitate the *in situ* identification of targeted dendrites and synapses in different imaging modalities and to make 3D-CLEM more accessible to the neuroscientific community.

Here, we have developed a CLEM workflow combining confocal light microscopy with serial block-face scanning EM (SBEM) and targeted photo-precipitation of 3,3-diaminobenzidine (DAB) to facilitate ROI recovery. We applied this workflow to reconstruct dendritic spines located exclusively on the basal dendrites of genetically-labelled PNs in layers 2/3 (L2/3) of the somatosensory cortex (SSC) of adult mice. We analyzed the variability of their ultrastructure and estimated the electrical resistance of their neck. We also examined the distribution and the morphology of inhibitory synapses. We specifically examined dendritic spines receiving both excitatory and inhibitory inputs, which represented 10% of all spines along basal dendrites. These dually-innervated spines (DiSs) exhibited wider heads and larger ePSDs than singly-innervated spines (SiSs), and they were more electrically isolated from the dendritic shaft than SiSs of comparable head size. We then used our measurements to constrain a multi-compartment model of synaptic signaling and compartmentalization in dendrites. We assessed the effects of individual excitatory and inhibitory signals on membrane voltage and calcium concentration depending on inhibitory synapse placement (i.e. on a spine head or on the dendritic shaft) and input timing. Our results challenge the view that spinous inhibition strictly vetoes single excitatory inputs and rather suggest that it fine-tunes calcium levels in DiSs. Our simulations indicate that a single inhibitory postsynaptic potential (IPSP) evoked in a DiS within 10 ms after an excitatory

postsynaptic potential (EPSP) can curtail the local increase of calcium concentration without affecting the amplitude of membrane depolarization. This decoupling effect could impact long-term synaptic plasticity in cortical circuits.

RESULTS

Combining light and electron microscopy to access the ultrastructure of targeted populations of dendritic spines in brain slices

In the cortex, the morphology and distribution of dendritic spines vary depending on cortical area and layer in which the cell body is located [5,35,58,59], and dendritic spines are differently regulated depending on their location within dendritic trees — e.g. basal or apical dendrites [30,49,60–62]. Therefore, it is critical to take into account both the cellular and dendritic context to characterize the diversity of spine ultrastructure. To that aim, we developed a 3D-CLEM workflow allowing the ultrastructural characterization of dendritic spines on genetically-defined neuronal cell types and along identified types of dendrites in intact cortical circuits. In order to label specific subtypes of neurons, we used cortex-directed *in utero* electroporation (IUE) in mice. We electroporated neuronal progenitors generating layer 2/3 cortical PNs at embryonic day (E)15.5 with a plasmid expressing the fluorescent cytosolic filler tdTomato, granting access to the morphology of electroporated neurons, their dendrites and their dendritic spines in LM. We perfused adult mice with aldehyde fixatives, and collected vibratome sections of the electroporated area. To facilitate sample handling, we designed custom-made chambers allowing sample immersion in different solutions during confocal imaging and subsequent retrieval of the sample before EM preparation steps (S1 Fig). We enclosed 10-20 mm^2 fragments of brain sections in these chambers and acquired images of optically isolated basal dendrites of bright electroporated neurons with confocal microscopy (Fig 1A).

A major challenge of CLEM in brain tissue is to recover the ROI in EM after imaging in LM. Several methods have been proposed to facilitate ROI recovery [50–52], but they come with caveats: (1) using only intrinsic landmarks has a low throughput [57,63]; (2) filling

target neurons with 3,3-diaminobenzidine (DAB) masks intracellular ultrastructure [64]; (3) scarring the tissue with an infra-red laser to generate extrinsic landmarks, a.k.a. "NIRB" for "near-infrared branding" [56,65–68], produces landmarks with low pixel intensity in EM and can damage ultrastructure [63,69]. To facilitate ultrastructural measurements in non-obscured identified dendrites, we took advantage of the photo-oxidability of DAB [70,71]. We immersed the samples in DAB solution and applied focalized UV light at user-defined positions (Fig 1A) to imprint osmiophilic DAB landmarks around targeted dendrites (see panels B-E in S1 Fig) and pattern the tissue with localized electron-dense DAB precipitates (Fig 1B). After sample retrieval (see panel F in S1 Fig), tissue sections were processed for SBEM and embedded in minimal amounts of epoxy resin in order to maximize sample conductivity and SBEM image quality (see Methods). In 3D-EM stacks, ROIs were recovered within the complex environment of brain tissues using both intrinsic landmarks such as blood vessels (Fig 1B) and high-contrast DAB precipitates (Fig 1C; see also panel G in S1 Fig). We then segmented and reconstructed targeted dendrites in 3D, and registered whole portions of dendrites in both LM and EM to identify each dendritic spine unequivocally using neighboring spines as dependable topographic landmarks (Fig 1D). CLEM-based 3D-reconstruction enabled the identification of dendritic spines that were not visible in LM or EM alone. In LM, the limited axial resolution prevents the identification of axially oriented spines, which are easily detected in 3D-EM [49] (Fig 1D). On the other hand, spines with the longest and thinnest necks are conspicuous in LM stacks, but can be difficult to find in 3D-EM datasets without the cues provided by LM. The proportion of spines recovered with CLEM versus LM alone could amount to up to 30% per ROI, and 5% per ROI versus EM alone, highlighting the advantage of CLEM over unimodal microscopy approaches.

Spine ultrastructure along the basal dendrites of L2/3 cortical pyramidal neurons.

We used our CLEM workflow to quantify the full extent of the ultrastructural diversity of dendritic spines along the basal dendrites of layer 2/3 PNs of the SSC of three adult mice. We exhaustively segmented 254 µm of the basal dendritic arborization of four neurons and

we reconstructed a total of 390 individual spines (S1 Table). As spine distance to the soma spanned from 20 to 140 µm, with basal dendrites extending up to 150 µm [72–75], our dataset can be considered representative of the whole spine population on these dendrites. The average linear density of dendritic spines was 1.5 ± 0.3 spine.µm^{-1}. We then quantified the following parameters for each spine: neck length, neck diameter, head volume, head longitudinal diameter (referred to as "head length"), head orthogonal diameter (referred to as "head diameter"), number of PSDs, and PSD area (Fig 2A; S2 Table). In agreement with previous reports in both basal and apical dendrites of mouse cortical and hippocampal neurons [4,6,76,77], we found that ePSD area correlates linearly with the volume of the spine head (Fig 2B). We also observed a non-linear correlation between the length of the spine neck and its diameter (Fig 2C): long spines (neck length > 2 µm) always had thin necks (neck diameter < 0.2 µm), although short necks could also be thin. Furthermore, in spines with long necks, spine heads were always stretched longitudinally with respect to the neck (i.e. prolate) whereas they could also be stretched orthogonally (i.e. oblate) in shorter spines (Fig 2D), with a possible impact on nanoscale ion flows [78]. By contrast, there was no correlation between the position of the spine or the inter-spine distance and any of the morphological parameters we measured (S2 Fig). There was also no correlation between the length or the diameter of the neck and the morphometry of the spine head or ePSD (S1 Data), which is consistent with previous EM studies of L2/3 PNs of mouse neocortex [4,72] (but see [40,79] for different conclusions in other brain areas).

Since our CLEM approach grants access to the cytosolic content of spines (Fig 3A), we quantified the occurrence of SA, a complex stacked-membrane specialization of smooth endoplasmic reticulum (SER) which contributes to calcium signaling, integral membrane protein trafficking, local protein synthesis, and synaptic plasticity [12–14,80,81]. In basal dendrites, about 54% of spines contained a SA (Fig 3B), which is substantially higher than previous reports in the mature hippocampus [12,82]. These spines were randomly distributed along the dendrites. They had larger heads (Fig 3C), larger ePSDs (Fig 3D) and wider necks than spines devoid of SA (Fig 3E), consistent with previous morphological

192 studies of CA1 PNs [12,82,83]. The probability that a spine contained a SA depending on
193 spine head volume followed a sigmoid model (Fig 3F), predicting that all spines with a head
194 diameter larger than 1.1 µm (21% spines in our reconstructions) contain a SA.

195 Next, we used our ultrastructural data to estimate the electrical resistance of spine
196 necks using $R_{neck} = \rho W_{neck}$, where ρ is the cytosolic resistivity (set to 300 Ω.cm [84,85]) and
197 W_{neck} is the diffusional neck resistance that restricts the diffusion of molecules and charges
198 between spine heads and dendritic shafts [23]. To quantify W_{neck}, for each spine we
199 measured a series of orthogonal cross-sections of the neck along its principal axis and
200 integrated $W_{neck} = \int d\ell / A(\ell)$, where $A(\ell)$ is the neck cross-section area at the abscissa ℓ
201 along the neck axis. W_{neck} ranged from 2 μm^{-1} to 480 μm^{-1} and R_{neck} from 8 MΩ to 1450 MΩ,
202 with a median value of 188MΩ. These values are consistent with previous estimations based
203 on EM reconstructions and STED super-resolutive light microscopy [17,86], and with direct
204 electrophysiological recordings [87]. It has been proposed that the spine apparatus, which
205 may occupy some of the spine neck volume, could increase W_{neck} [13,80,88]. Therefore, we
206 subtracted SA cross-section from $A(\ell)$ when computing W_{neck} in SA+ spines (see Methods).
207 This correction increased W_{neck} by 13% ± 2% in SA+ spines (S3 Fig). However, because of
208 their wider necks, W_{neck} of SA+ spines was still lower (59% in average) than W_{neck} of spines
209 devoid of SA (Fig 3G). These results suggest that, in addition to supplying large dendritic
210 spines with essential resources, the SA may adjust W_{neck} and influence spine
211 compartmentalization [12,13,82].
212
213 **Excitatory and inhibitory synapses in dually-innervated spines.**
214 We noticed that a small proportion of dendritic spines were contacted by two distinct pre-
215 synaptic boutons (DiSs). DiSs have long been described in the literature as receiving both
216 an excitatory and an inhibitory synaptic contact [89–92]. In the somato-sensory cortex, DiSs
217 are contacted by VGLUT2-positive thalamocortical inputs [15] and they are sensitive to
218 sensory experiences. The number of DiSs increases in response to sensory stimulation and
219 decreases in response to sensory deprivation [73,93–95], suggesting their importance in

synaptic integration and sensory processing. However, their scarcity in the cortex has been an obstacle to their ultrastructural and functional characterization. We took advantage of our CLEM approach and the molecular signature of this population of spines (i.e. the presence of a cluster of gephyrin, the core protein of inhibitory postsynaptic scaffolds [96,97]) to examine their morphological properties. To label inhibitory synapses in cortical PNs (Fig 4A), we co-expressed tdTomato with small amounts of GFP-tagged gephyrin (GFP-GPHN) [73,95,98,99]. We identified in LM spines containing a gephyrin cluster (Fig 4B) and we ascertained their dual-innervation in EM after back-correlating spine identity between LM and SBEM acquisitions. To do so, we aligned reconstructed dendrites on LM images (Fig 4C) and matched individual spines in both modalities (lettered in Fig 4B and Fig 4C). While ePSDs look asymmetrical and more electron-dense than inhibitory PSDs (iPSDs) in transmission EM [100,101], the anisotropic resolution of SBEM does not allow the distinction of ePSDs and iPSDs in most DiSs [49]. Therefore, we identified iPSDs on DiSs based on GFP-GPHN cluster position in LM images. In 89% of DiSs (33/37), the excitatory (GFP-GPHN-negative) PSD and the inhibitory (GFP-GPHN-positive) PSD could be clearly discriminated. However, in 11% of DiSs (4/37 DiSs), distinguishing ePSD from iPSD was not obvious due to the coarse axial resolution of LM imaging. To resolve ambiguities, we reconstructed the axons innervating the DiSs and determined their identity based on their other targets in the neuropil, either soma and dendritic shaft for inhibitory axons [2,102,103], or other dendritic spines for excitatory axons [49] (Fig 4D). As a result, we could unequivocally determine the excitatory or inhibitory nature of each synaptic contact on electroporated neurons, within ~10^5 μm^3 3D-EM acquisition volume.

In CLEM, we measured an average density of 1.4 ± 0.5 iPSDs per 10 µm of dendrite on DiSs and 2.1 ± 1.2 iPSDs per 10 µm of dendrite on the dendritic shaft— amounting to 3.5 ± 1.1 iPSDs per 10 µm of dendrite. iPSDs were homogeneously distributed either on spines or shaft from 24 µm away from the soma to the dendritic tip, which contrasts with apical dendrites where spinous inhibitory synapses are distally enriched [73]. Along the basal dendrites of L2/3 cortical PNs, 38% of inhibitory contacts occurred on dendritic spines, which

is higher than previously estimated using LM only [73,99]. DiSs represented 10% ± 3% of all spines (Fig 5A). They had larger heads than SiSs (Fig 5B), in line with previous reports [15,104], and 86% ± 13% of them contained a SA (Fig 5C). DiSs also differed in terms of neck morphology. They had longer necks than SiSs of comparable head volume (V_{head} > 0.05 μm^3), although neck length distribution was similar in the whole populations of SiSs and DiSs (Fig 5D). DiSs also had lower D_{neck}/V_{head} ratio than SiSs (Fig 5E), although D_{neck} distribution was similar between SiSs and DiSs (S4 Fig), suggesting that excitatory signals generated in DiSs are more compartmentalized than signals of similar amplitude generated in SiSs. Accordingly, DiSs had a higher W_{neck} than SiSs of comparable head size (52% larger in average) (Fig 5F). In spine heads, ePSDs on DiSs were larger than ePSDs on SiSs (174% ± 113% of ePSD area) (Fig 5G), consistent with the larger head size of DiSs. By contrast, iPSDs on DiSs were smaller than shaft iPSDs (53% ± 15% of shaft iPSD area) (Fig 5H). The area of iPSDs on DiSs did not correlate with spine head volume (S5 Fig). In 95% of DiSs, iPSDs were smaller than ePSDs (half the area, in average) (Fig 5I). Together, these results indicate that DiSs represent a specific population of dendritic spines with distinctive ultrastructural features that could impact their functional properties.

Morphologically constrained model of synaptic signaling

Next, we wanted to assess the impact of spine diversity on synaptic signals. We used a computational approach based on a multi-compartment "ball-and-stick" model of the neuronal membrane [40,105]. This model comprises an isopotential soma and two dendritic compartments structured as cables featuring passive resistor-capacitor (RC) circuits and conductance-based synapses. The two dendritic compartments correspond to the dendrite receiving the synaptic inputs and to the remainder of the dendritic tree (Fig 6A1) [106,107]. We constrained this model with morphological parameters measured in CLEM (i.e. distance between spine and soma, neck resistance, head volume, head membrane area, ePSD area and iPSD area for 390 spines, and dendritic diameter), taking into account the structural shrinkage resulting from chemical fixation (S6 Fig). Excitatory and inhibitory synaptic

conductances were modeled as bi-exponential functions of time, with their rise and decay times tuned to the kinetics of different receptor types: AMPA and NMDA receptors at ePSDs, and type A γ-aminobutyric acid ($GABA_A$) receptors at iPSDs (Fig 6A2; see Methods). Individual synaptic conductances were scaled proportionally to PSD areas [9,77,108]. Voltage-dependent calcium channels (VDCCs) in spine heads were modeled using Goldman–Hodgkin–Katz equations [109] and their conductance was scaled proportionally to spine head areas. We adjusted excitatory synaptic conductivity so that average amplitudes of both synaptic currents and somatic depolarizations evoked by individual excitatory postsynaptic potentials (EPSPs) fitted published electrophysiological values [110–113] (see Methods). After calibration of excitatory synapses, maximal synaptic conductance (g) ranged from 0.04 nS to 3.13 nS for g_{AMPA} (0.456 ± 0.434 nS) and from 0.04 nS to 3.42 nS for g_{NMDA} (0.498 ± 0.474 nS), in line with the literature [114]. We then adjusted inhibitory synaptic conductivity to set the mean conductance of dendritic inhibitory synapses to 1 nS [37,115,116]. As a result, g_{GABA} ranged from 0.33 nS to 3.36 nS (1.00 ± 0.577 nS) for synapses located on the shaft, and from 0.19 nS to 1.56 nS (0.528 ± 0.277 nS) for inhibitory synapses located on spines.

We first examined the propagation of simulated EPSPs. We compared the evoked depolarization amplitude ΔV_{max} in three different compartments: in the spine head in which the EPSP was elicited, in the dendritic shaft close to the spine, and in the soma (Fig 6B). ΔV_{max} followed a log-normal distribution, reflecting the morphological variability of spines (Fig 6B). Due to the passive attenuation of electrical signals along dendritic processes, ΔV_{max} was sharply attenuated between the head of the spine and the dendritic shaft (51% attenuation in average) and about 5% of ΔV_{max} reached the soma (Fig 6B), in line with measurements performed in basal dendrites of L5 cortical PNs using voltage dyes, electrophysiology and glutamate uncaging [25,117]. ΔV_{max} scaled with ePSD area in all compartments (Fig 6C). To determine the contribution of morphological parameters to the variance of ΔV_{max}, we used a generalized linear model (GLM) [118]. We analyzed the contribution of the volume, diameter and resistance of spine necks and heads as well as the

304 contribution of ePSD area and distance between spine and soma (L_{dend}) to the amplitude of
305 the signals in the soma and in spine heads. In the soma, ΔV_{max} was mainly determined by
306 A_{ePSD}, which accounted for 89% of its variance when EPSPs were elicited in SiSs (77%
307 when they came from DiSs). The second determinant was L_{dend}, which accounted for 6.4% of
308 the variance of ΔV_{max} for EPSPs generated in SiSs (14.7% in DiSs). The contribution of R_{neck}
309 to the variance of ΔV_{max} in the soma was comparatively negligible (S3 Table), indicating that
310 the passive attenuation of EPSPs along dendrites dominates the contribution of R_{neck} to
311 somatic depolarizations evoked in spines. In the heads of SiSs, A_{ePSD} and R_{neck} accounted
312 for 60% and 19% of the variance of ΔV_{max}, respectively (also see S7 Fig for the dependence
313 of ΔV_{max} on R_{neck}). In the heads of DiSs, the contribution of R_{neck} to ΔV_{max} was much higher,
314 reaching 38% of the variance, while A_{ePSD} contribution dropped to 47% (S3 Table). In 56% of
315 dendritic spines, R_{neck} was large enough (>145MΩ) to attenuate EPSP amplitude by >50%
316 across the spine neck, and more than 90% of spine necks attenuated the signal by at least
317 10% (Fig 6D), suggesting that most spine necks constitutively compartmentalize electrical
318 signals in the head of spines.

319 We also estimated the elevation of calcium ion concentration ($\Delta[Ca^{2+}]$) in spine heads
320 induced by an EPSP. $\Delta[Ca^{2+}]$ was similar in SiSs and DiSs and varied non-linearly with A_{ePSD}
321 (Fig 6E). A_{ePSD} was the main determinant of $\Delta[Ca^{2+}]$, accounting for 30% of the variance in
322 SiSs (45% in DiSs), followed by R_{neck} (9%; S3 Table). As a single EPSP is not sufficient to
323 elicit a Ca^{2+} spike, we did not model Ca^{2+} transients outside of spine heads. Overall, our
324 model provides quantitative insights into the variability of EPSP amplitude originating from
325 spine diversity and highlights differences in the contribution of morphological parameters to
326 spine depolarization and calcium signals in DiSs and SiSs.
327
328 **Spatial interplay of excitatory and inhibitory signals**
329 We used our model to compare the effects of spinous and dendritic shaft inhibition. *In vitro*
330 uncaging experiments have shown that inhibitory contacts located on DiSs could weaken
331 local calcium signals [119], but the consequences on synaptic excitation are still unclear

[75,120]. To understand how spine ultrastructure and iPSD location influence synaptic integration, we modeled the interaction between one IPSP and one EPSP under the constraint of our morphological measurements. Assessing the extent of signal variability originating from spine morphological heterogeneity requires a large number of simulations (N≥1000). Therefore, we used a bootstrapping method [121] (see Methods) to derive N≥1000 sets of parameters from our dataset of 390 spines and 62 shaft iPSDs (S1 Data), and provide unbiased estimations of the mean and variance of the signals. Importantly, the strength of inhibition depends on the reversal potential of chloride ions (E_{Cl^-}). In healthy mature layer 2/3 cortical PNs, E_{Cl^-} typically varies between the resting membrane potential, V_{rest} = -70 mV, and hyperpolarized values (-80 mV) [122]. When E_{Cl^-} = -70 mV, active inhibitory synapses generate a local increase of membrane conductance, which "shunts" membrane depolarization induced by concomitant EPSPs. When E_{Cl^-} < -70 mV, the driving force of Cl^- ions is stronger, GABAergic inputs can hyperpolarize the cell membrane and IPSPs counter EPSPs. These two situations are respectively termed "shunting inhibition" and "hyperpolarizing inhibition" [37,122].

We first assessed the impact of "shunting" IPSPs elicited in the dendritic shaft on individual EPSPs depending on the inter-synaptic distance (Fig 7A). For each iteration of the model (i.e. N=3700 sets of realistic morphological values for spine size, and iPSD location and size), we varied the distance Δx between a spine receiving an EPSP and a shaft iPSD activated simultaneously. For $\Delta x > 0$, the iPSD was located between the spine and the soma (i.e. "on-path" inhibition, from the viewpoint of the soma), and for $\Delta x < 0$, the iPSD was located distally to the spine (i.e. "off-path" inhibition). To quantify inhibition, we compared the amplitude of individual EPSPs in the absence ($\Delta V_{max,E}$) or presence ($\Delta V_{max,E+I}$) of inhibition, and computed the drop in depolarization amplitude $inh_V = 1 - \Delta V_{max,E+I} / \Delta V_{max,E}$. $inh_V = 0$ indicates that the electrical signal was not affected, $inh_V = 1$ indicates that it was completely inhibited. Importantly, due to the electrical properties of the cell membrane, inh_V depends on where the signal is measured. In the soma, inh_V was maximal (20% in average) when the iPSD was located on-path and it decreased exponentially with Δx when the iPSD was

360 located off-path (exponential decay length: $L_{soma,off}$ = 30 μm) (Fig 7B), highlighting the impact
361 of proximal inhibitory synapses on distal excitatory inputs [37,123]. In the spine where the
362 EPSP was elicited, inh_V decayed exponentially with Δx for both on-path and off-path
363 inhibition (Fig 7C), with respective decay lengths $L_{spine,on}$ = 30 µm and $L_{spine,off}$ = 11 µm (also
364 see S8 Fig for the dependence of decay lengths on the dendritic cross-section). Therefore,
365 shaft inhibition could affect excitatory signals within 40 µm, which corresponds to
366 approximately 50 spines considering the spine density and dendritic diameter that we
367 measured in basal dendrites of L2/3 cortical PN.

368 Next, we focused on DiSs. We modeled N=3700 DiSs and shaft iPSDs (Δx = 0) at
369 random locations on the dendrite, and we compared two configurations per iteration of the
370 model: (1) the ePSD of the DiS and the shaft iPSD were activated simultaneously (Fig 8A1);
371 (2) both the ePSD and the iPSD of the DiS were activated simultaneously (Fig 8A2). In the
372 soma, the effect of shaft and spinous inhibition was comparable: inh_V was centered on 17%,
373 and reached up to 50% (Fig 8B), in line with somatic recordings following coincident
374 uncaging of glutamate and GABA in acute brain slices [119]. By contrast, in the head of all
375 DiSs, spinous inhibition was more efficient than shaft inhibition despite the smaller size of
376 spinous iPSDs compared to shaft iPSDs. Spinous inh_V was centered on 10% and reached
377 up to 35%, whereas dendritic inh_V was centered on 3% and did not reach more than 23%
378 (Fig 8C). These results support the notion that the placement of inhibitory synapses
379 structures the detection and integration of excitatory signals [103,124,125], and highlight the
380 role of spinous inhibition in local synaptic signaling.

381 We then run the simulations with a lower chloride reversal potential (E_{Cl^-} = -80 mV)
382 for which GABAergic inputs can hyperpolarize the cell membrane. In numerous simulations,
383 we observed that hyperpolarization could take over depolarization (i.e. $inh_V > 1$) (see panel A
384 in S9 Fig). This was the case in the soma for 37% of simulations, and in the spine where the
385 EPSP was generated for 10% of simulations. With E_{Cl^-} = -80 mV, the median inh_V imposed
386 by spinous inhibition in spine heads was 45%, in line with a previous morphologically
387 constrained model [75] and with the fact that a hyperpolarizing IPSP may block multiple

EPSPs depending on iPSD placement [103]. Interestingly, lowering E_{Cl}- affected spinous and shaft inhibition differently. In the soma, shaft inhibition became more efficient than spinous inhibition (see panel B in S9 Fig) due to the larger area of shaft iPSDs. However, in the heads of most DiSs, spinous inhibition remained more efficient than shaft inhibition (see panels C-F in S9 Fig). Altogether, our results indicate that spinous inhibition is stronger than shaft inhibition in DiSs, and that their relative weight is modulated by the driving force of chloride ions.

Temporal interplay of excitatory and inhibitory signals

Since the efficacy of inhibition depends on the membrane potential at the onset of the IPSP [36,38,123,126], we addressed the effect of input timing on inhibition efficacy in DiSs. We simulated the interaction of one EPSP and one IPSP generated with a time difference of Δt (Fig 9A). For $\Delta t < 0$ (IPSP before EPSP), IPSPs decreased ΔV_{max} (Fig 9B1). For $\Delta t > 0$ (IPSP after EPSP), IPSPs had no effect on ΔV_{max} but abruptly decreased the tail of the EPSPs [126] (Fig 9B2). We first compared how spinous and shaft inhibition reduced EPSP duration by comparing the 80-to-20% decay time of the summed signals (τ_{E+I}) to that of uninhibited EPSPs (τ_E). Decay times were minimal at Δt = +4 ms and decreased by 64% and 78% with spinous and shaft inhibition respectively (Fig 9C), which could shorten the integration window of EPSPs and increase the temporal precision of synaptic transmission [127]. The variance of τ_E was mainly determined by the area of iPSDs (S4 Table). We then quantified how the timing of inhibition affected EPSP amplitude using $inh_V(\Delta t) = 1 - \Delta V_{max,E+I} / \Delta V_{max,E}$. In spine heads, inh_V was an asymmetrical function of Δt [36,126] and it was maximal at Δt = -4 ms for spinous inhibition, and at Δt = -6 ms for dendritic shaft inhibition. Overall, spinous inhibition was stronger than shaft inhibition, decreasing ΔV_{max} by 26.3% and 16.2%, respectively (median values in Fig 9D; see also panel A in S10 Fig for inh_V (Δt) with higher E_{Cl}-). Interestingly, R_{neck} had a negligible contribution to the variance of inh_V in the case of

hyperpolarizing inhibition, but a major one (37%) in the case of shunting inhibition (S4 Table), suggesting that spine necks compartmentalize IPSPs differently depending on E_{Cl^-}.

Then, we examined the effect of timed inhibition on calcium signaling in spines, using $inh_{[Ca^{2+}]}(\Delta t) = 1 - [Ca^{2+}]_{max,E+I} / [Ca^{2+}]_{max,E}$. We observed that $inh_{[Ca^{2+}]}$ peaked at $\Delta t = 0$ ms for both spinous and shaft inhibition. More precisely, spinous inhibition reduced calcium transient amplitude by 10% in average, reaching >36% in the top 10% simulations, while shaft inhibition reduced it by 8.6% in average and >28% in the top 10% simulations (Fig 9E). These values are in the range of $inh_{[Ca^{2+}]}$ measured with double uncaging experiments [119]. Importantly, IPSPs could decrease the amplitude of calcium transients, within a short time-window (Δt between 0 and +10 ms) in which depolarization amplitude was not affected (Fig 9D-E), thereby decoupling calcium signalling from electrical activity in DiSs.

DISCUSSION

In the present study, we developed a novel 3D-CLEM workflow allowing the ultrastructural characterization of specific populations of dendritic spines in genetically defined types of neurons. We used this workflow to exhaustively reconstruct spines and synaptic contacts along the basal dendrites of fluorescently labelled L2/3 cortical PNs of the SSC and to provide a quantitative description of their diversity. We input our measurements in a computational model to analyze the variability of electrical and calcium synaptic signals originating from spine ultrastructural diversity, and to characterize the spatio-temporal integration of excitatory and inhibitory inputs. Our results shed light on unique properties of DiSs, which represent 10% of all spines and 38% of all inhibitory synapses along the basal dendrites of L2/3 cortical PNs. We show that while individual inhibitory synapses distributed along dendritic shafts can be powerful enough to block several EPSPs, spinous inhibitory synapses affect excitatory signals more efficiently in DiSs. We also show that the activation of a spinous inhibitory synapse within a few milliseconds after an EPSP can decouple voltage and calcium signals in DiSs, which could impact calcium-dependent signaling cascades that drive spine plasticity.

442 The molecular composition of synapses and their biophysical properties are
443 reportedly heterogeneous along dendrites and across dendritic trees [35,39,128,129].
444 However, most computational models so far have used *ad hoc* or averaged values as
445 parameters for dendritic spines and excitatory synapses [130–132], and considered that all
446 inhibitory synapses were located along the dendritic shaft [133]. The correlative approach we
447 propose provides an accessible solution for detailed quantification of synaptic diversity
448 beyond the µm scale in intact brain circuits, which may help improve the accuracy of
449 computational models. Our workflow is applicable to any type of tissue and allows
450 anatomical measurements of any kind of genetically labelled cells and organelles. One
451 technical limitation is the need for chemical fixation, which may distort tissue morphology
452 [134,135]. Therefore, it may be necessary to correct for tissue shrinkage based on a
453 morphological comparison with physically fixed tissues (see panel B3 in S6 Fig) in order to
454 reliably depict *in vivo* situations. Future development of aldehyde-free cryo-CLEM methods
455 will be important to grant access to cellular and synaptic ultrastructure in close-to-native
456 environments.

457 Applying 3D-CLEM to the basal dendrites of L2/3 cortical PNs allowed us to
458 quantitatively describe the landscape of synaptic diversity and to characterize the
459 ultrastructural features of a scarce population of dendritic spines receiving both excitatory
460 and inhibitory synaptic inputs (DiSs). In the cortex, DiSs are mostly contacted by VGluT2-
461 positive excitatory thalamo-cortical inputs [15] and they receive inhibition from somatostatin-
462 expressing and parvalbumin-expressing interneurons [119,136], which are the two main
463 sources of inhibitory inputs to the basal dendrites of layer 2/3 cortical PNs [137,138]. *In vivo*
464 2-photon imaging experiments have shown that DiSs are among the most stable spines
465 along the dendrites of layer 2/3 PNs [104]. The inhibitory synapse in DiSs is smaller and
466 more labile than inhibitory synapses along dendritic shafts, and it is very sensitive to sensory
467 experience [73,94,95,104]. Whisker stimulation induces a lasting increase in the occurrence
468 of iPDSs in spines of the barrel cortex [94] and monocular deprivation destabilizes iPSDs
469 housed in spines of the visual cortex [73,95,104], suggesting their role in experience-

dependent plasticity. Our morphological and computational analysis provides new insights into the biophysical properties of DiSs. We show that DiSs have larger heads and larger ePSDs than SiSs, and most often contain a spine apparatus. However, the ratio between mean spine neck diameter and spine head volume (or ePSD area) was smaller in DiSs than in SiSs, and DiSs had longer necks than SiSs of comparable head volume, so that EPSPs of similar amplitudes encounter a higher neck resistance in DiSs than in SiSs. Thus, DiSs are uniquely compartmentalized by their ultrastructural features and the presence of an inhibitory synapse.

Our model predicts that IPSPs occurring in DiSs within milliseconds after an EPSP can curtail calcium transients without affecting depolarization, thereby locally decoupling voltage and calcium signaling. This is expected to impact the induction of long-term forms of synaptic plasticity, such as long-term potentiation (LTP) or long-term depression (LTD), which underlie learning and memory [80,139–141]. The induction of LTP versus LTD is determined by the magnitude and time course of calcium flux, with brief, high calcium elevation generating LTP, sustained moderate calcium elevation generating LTD, and low calcium level inducing no plasticity [142–144]. Therefore, a small reduction in the amplitude of calcium transients may limit spine potentiation, or even cause depression [120,145,146]. In the cortex, thalamocortical inputs may contact DiSs on the basal dendrites of L2/3 both directly (excitatory connection) and indirectly through feed-forward inhibition *via* parvalbumin-expressing fast-spiking interneurons [127,147]. The delay between thalamo-cortical excitatory and feed-forward inhibitory signals is typically +1 ms to +3 ms [127], within the 10 ms time window for voltage-calcium decoupling in DiSs. Therefore, the presence of inhibitory synapses in DiSs could prevent synaptic potentiation and thereby increase the temporal precision of cortical response to sensory stimulation [94,127,148]. On the contrary, the removal of spine inhibitory synapses could favor synaptic potentiation during experience-dependent plasticity such as monocular deprivation to strengthen inputs from the non-deprived eye [73,95,149].

Our understanding of synaptic and dendritic computations is intimately linked to the quantitative description of synaptic distribution, ultrastructure, nano-organization, activity and diversity in neural circuits. The CLEM workflow we propose opens new avenues for the ultrastructural characterization of synapses with defined molecular signature characterizing their identity or activation profile in response to certain stimuli or behaviors. Another milestone to better model the biophysics of synaptic integration will be to combine EM and quantitative super-resolution LM to measure the density and nano-organization of molecular species (e.g. AMPARs, NMDARs, voltage-dependent calcium channels) in specific populations of synapses in intact brain circuits. Combining circuit and super-resolution approaches through CLEM will be critical to refine large-scale circuit models [74,133,150] (but see [32]) and bridge the gap between molecular, system and computational neurosciences.

MATERIALS AND METHODS

Animals and *in utero* cortical electroporation

All animals were handled according to French and EU regulations (APAFIS#1530-2015082611508691v3). *In utero* cortical electroporation was performed as described previously [151]. Briefly, pregnant Swiss female mice at E15.5 (Janvier Labs, France) were anesthetized with isoflurane (3.5% for induction, 2% during the surgery) and subcutaneously injected with 0.1 mg/kg of buprenorphine for analgesia. The uterine horns were exposed after laparotomy. Electroporation was performed using a square wave electroporator (ECM 830, BTX) and tweezer-type platinum disc electrodes (5mm-diameter, Sonidel). The electroporation settings were: 4 pulses of 40 V for 50 ms with 500 ms interval. Endotoxin-free DNA was injected using a glass pipette into one ventricle of the mouse embryos at the following concentrations: pH1SCV2 TdTomato: 0.5 µg/µL and pCAG EGFP-GPHN: 0.3 µg/µL. All constructs have been described before [98].

Cortical slice preparation

Electroporated animals aged between postnatal day P84 and P129 were anesthetized with ketamin 100 mg/kg and xylazin 10 mg/kg, and intracardiacally perfused with first 0.1 mL of heparin (5000 U.I/mL, SANOFI), then an aqueous solution of 4% w/v paraformaldehyde (PFA) (Clinisciences) and 0.5% glutaraldehyde (GA) (Clinisciences) in 0.1 M phosphate-buffered saline (PBS). The fixative solution was made extemporaneously, and kept at ice-cold temperature throughout the perfusion. The perfusion was gravity-driven at a flow rate of about 0.2 ml/s, and the total perfused volume was about 100 ml per animal. Brains were collected and post-fixed overnight at 4°C in a 4% PFA solution. 30 µm-thick coronal brain sections were obtained using a vibrating microtome (Leica VT1200S).

Fluorescence microscopy of fixed tissue

Slices containing electroporated neurons were trimmed to small (5-10 mm^2) pieces centered on a relatively isolated fluorescent neuron, then mounted in a custom-made chamber on #1.5 glass coverslips. The mounting procedure consisted in enclosing the slices between the glass coverslip and the bottom of a cell culture insert (Falcon, ref. 353095) adapted to the flat surface with a silicon O-ring gasket (Leica) and fixed with fast-curing silicon glue (see panel A in S1 Fig). Volumes of GFP and tdTomato signals were acquired in 12 bits mode (1024x1024 pixels) with z-steps of 400 nm using an inverted Leica TCS SP8 confocal laser scanning microscope equipped with a tunable white laser and hybrid detectors and controlled by the LAF AS software. The objective lenses were a 10X PlanApo, NA 0.45 lens for identifying electroporated neurons and a 100X HC-PL APO, NA 1.44 CORR CS lens (Leica) for higher magnification images. GFP-GPHN puncta with a peak signal intensity at least four times above shot noise background levels were considered for CLEM.

Placement of DAB fiducial landmarks

Following confocal imaging, slices were immersed in a solution of 1 mg/mL 3,3'-diaminobenzidine tetrahydrochloride (DAB, Sigma Aldrich) in Tris buffer (0.05 M, pH 7.4). The plugin “LAS X FRAP” (Leica) was used to focus the pulsed laser in the tissue in custom

patterns of 10-to-20 points using 100% power in 4 wavelengths (470 to 494nm) for 30s-60s per point at 3 different depths: the top of the slice, the depth of the targeted soma, then the bottom of the slice (surface closest to the objective). DAB precipitates were imaged in transmitted light mode. Slices were subsequently rinsed twice in Tris buffer and prepared for electron microscopy.

Tissue preparation for serial block-face scanning electron microscopy (SBEM)

Using a scalpel blade under a M165FC stereomicroscope (Leica), imaged tissue slices were cut to ~1mm^2 asymmetrical pieces of tissue centered on the ROI, and then kept in plastic baskets (Leica) through the osmification and dehydration steps. Samples were treated using an osmium bridging technique adapted from the NCMIR protocol (OTO) [152]. The samples were washed 3 times in ddH_2O and immersed for 1 hour in a reduced osmium solution containing 2% osmium tetroxide and 1.5% potassium ferrocyanide in ddH_2O. Samples were then immersed for 20 minutes in a 1% thiocarbohydrazide (TCH) solution (Electron Microscopy Science) prepared in ddH_2O at room temperature. The samples were then post-fixed with 2% OsO_4 in ddH_2O for 30 minutes at room temperature and colored *en bloc* with 1% aqueous uranyl acetate at 4 °C during 12 hours. Post-fixed samples were subjected to Walton's *en bloc* lead aspartate staining at 60 °C for 30 minutes (Walton, 1979). After dehydration in graded concentrations of ice-cold ethanol solutions (20%, 50%, 70%, 90% and twice 100%, 5 minutes per step) the samples were rinsed twice for 10 minutes in ice-cold anhydrous acetone. Samples were then infiltrated at room temperature with graded concentrations of Durcupan (EMS) prepared without plastifier (components A, B, C only). In detail, blocks were infiltrated with 25% Durcupan for 30 minutes, 50% Durcupan for 30 minutes, 75% Durcupan for 2 hours, 100% Durcupan overnight, and 100% fresh Durcupan for 2 hours before being polymerized in a minimal amount of resin in a flat orientation in a sandwich of ACLAR® 33C Films (EMS) at 60 °C for 48 hours. Samples were mounted on aluminum pins using conductive colloidal silver glue (EMS). Before curing, tissue blocks were pressed parallel to the pin surface using a modified glass knife with 0° clearance angle

581 on an ultramicrotome (Ultracut UC7, Leica), in order to minimize the angular mismatch
582 between LM and SEM imaging planes. Pins then cured overnight at 60°C. Samples were
583 then trimmed around the ROI with the help of fluorescent overviews of the ROI within their
584 asymmetrical shape. Minimal surfacing ensured that superficial DAB landmarks were
585 detected at the SBEM before block-facing.
586
587 **SBEM acquisition**
588 SBEM imaging was performed with a Teneo VS microscope (FEI) on the ImagoSeine
589 imaging platform at Institut Jacques Monod, Paris. The software MAPS (Thermo Fisher
590 Scientific) was used to acquire SEM images of targeted volumes at various magnifications.
591 Acquisition parameters were: 1,7830 kV, 500 ns/px, 100 pA, 40 nm-thick sectioning and
592 8200x8200 pixels resolution with either 2.5 nm or 25 nm pixel size for high- and low-
593 magnification images, respectively. Placing an electromagnetic trap above the diamond
594 knife to catch discarded tissue sections during days-long imaging sessions was instrumental
595 to achieve continuous 3DEM acquisitions.
596
597 **Image segmentation**
598 Dendrites were segmented from SBEM stacks using the software Microscopy Image
599 Browser (MIB) [153]. 3D reconstruction was performed with the software IMOD [154]
600 (http://bio3d.colorado.edu/imod/). 3D spine models were imported in the software Blender
601 (www.blender.org) for subsampling and the quantification of spine section areas along their
602 main axis was done with in-house python scripts. Other measurements were performed
603 using IMOD and in-house python scripts.
604
605 **Tissue preparation for tissue shrinkage estimation**
606 Two female mice (21 days postnatal) were used for the analysis of tissue shrinkage induced
607 by chemical fixation. Mice were decapitated and their brains were rapidly removed. The
608 brains were transferred to an ice-cold dissection medium, containing (in mM): KCl, 2.5;

609 $NaHCO_3$, 25; NaH_2PO_4, 1; $MgSO_4$, 8; glucose, 10, at pH 7.4. A mix of 95% O_2 and 5% CO_2
610 was bubbled through the medium for 30 min before use. 300-µm-thick coronal brain
611 sections were obtained using a vibrating microtome (Leica VT1200S). Small fragments of
612 the SSC were cut from those slices and fixed either by immersion in an ice-cold PBS
613 solution containing 4% PFA and 0.5% GA, or in frozen with liquid nitrogen under a pressure
614 of 2100 bars using a high pressure freezing system (HPM100, Leica). For HPF-frozen
615 samples, the interval between removal of the brain and vitrification was about 7 min. Cryo-
616 substitution and tissue embedding were performed in a Reichert AFS apparatus (Leica).
617 Cryo-substitution was performed in acetone containing 0.1% tannic acid at -90°C for 4 days
618 with one change of solution, then in acetone containing 2% osmium during the last 7h at -
619 90°C. Samples were thawed slowly (5°C/h) to -20°C and maintained at -20°C for 16
620 additional hours, then thawed to 4°C (10°C/h). At 4°C the slices were immediately washed
621 in pure acetone. Samples were rinsed several times in acetone, then warmed to room
622 temperature and incubated in 50% acetone-50% araldite epoxy resin for 1h, followed by
623 10% acetone-90% araldite for 2h. Samples were then incubated twice in araldite for 2h
624 before hardening at 60°C for 48h. As for chemically fixed sections, they were post-fixed for
625 30 min in ice-cold 2% osmium solution, rinsed in PBS buffer, dehydrated in graded ice-cold
626 ethanol solutions and rinsed twice in ice-cold acetone, before undergoing the same resin
627 infiltration and embedding steps as HPF-frozen samples. After embedding, ultrathin sections
628 were cut in L2/3 of the SSC, orthogonally to the apical dendrites of pyramidal neurons, 200-
629 300 µm from the pial surface using an ultramicrotome (Ultracut UC7, Leica). Ultra-thin (pale
630 yellow) sections were collected on formwar-coated nickel slot grids, then counterstained with
631 5% uranyl acetate in 70% methanol for 10 min, washed in distilled water and air dried before
632 observation on a Philips TECNAI 12 electron microscope (Thermo Fisher Scientific).
633
634 **Measurement of shrinkage correction factors**
635 Ultra-thin sections of both HPF-frozen tissues and chemically-fixed tissues were observed
636 using a Philips TECNAI 12 electron microscope (Thermo Fisher Scientific). Cellular

637 compartments contacted by a pre-synaptic bouton containing synaptic vesicles and
638 exhibiting a visible electron-dense PSD at the contact site, but no mitochondrion within their
639 cytosol were identified as dendritic spine heads. Cross-section areas of random spine heads
640 and the curvilinear lengths of their PSD were quantified in both conditions using the
641 softwares MIB and IMOD. N = 277 spine head sections were segmented in HPF-frozen
642 cortical slices from two female mice, and N = 371 spine head sections were segmented in
643 chemically fixed cortical slices originating from the same two mice. Chi-square minimization
644 was used between spine head cross-section area distributions in HPF or OTO conditions to
645 compute average volume shrinkage and correction factors. PSD areas were not corrected as
646 they exhibited no shrinkage.
647
648 **Computation of the diffusional neck resistance**
649 The diffusional resistance of spine necks W_{neck} was measured as follows. Using IMOD, we
650 first modeled in 3D the principal axis of each spine neck as an open contour of total length
651 L_{axis} connecting the base of the neck to the base of the spine head. Using Blender, we
652 interpolated each spine neck path linearly with 100 points. We named P(ℓ) the plane that
653 bisected the spine neck model orthogonally to the path at the abscissa ℓ, and A(ℓ) the spine
654 neck cross-section within P(ℓ). In spines containing a spine apparatus (SA), we corrected
655 A(ℓ) by a scaling factor $\beta(\ell) = 1 - (D_{SA}/D_{spine})^2(\ell)$, where $D_{SA}/D_{spine}(\ell)$ is the local ratio of SA
656 and neck diameter. We measured D_{SA}/D_{spine} orthogonally to the neck path in 10 SA+ spines
657 and in three different locations per spine on SBEM images: at the spine stem ($\ell/L_{axis} = 0.1$),
658 at the center of the spine neck ($\ell/L_{axis} = 0.5$), and at the stem of the head ($\ell/L_{axis} = 0.9$).
659 D_{SA}/D_{spine} was 44% ± 11%, 31% ± 8% and 37% ± 8% respectively, and fluctuations were not
660 statistically significant. We then divided each SA+ spine neck in thirds and scaled their neck
661 cross-section areas along neck axis $A_{SA+}(\ell) = \beta(\ell)A(\ell)$ before computing $W_{neck} = \int d\ell / A(\ell)$ for
662 all spines, using Simpson's integration rule.
663
664 **Multi-compartment electrical model**

All simulations were implemented in Python using NEURON libraries [155] and in-house scripts. Ordinary differential equations were solved with NEURON-default backward Euler method, with Δt = 0.05 ms. Scripts and model definition files are available in a GitHub repository: https://github.com/pabloserna/SpineModel. Biophysical constants were taken from the literature as follows: membrane capacitance C_m = 1µF/cm^2 [38]; cytosolic resistivity ρ = 300 Ω.cm [85,156]; synaptic conductivities were modeled as bi-exponential functions $g(t) = A\, g_{max} (e^{-t/t_2} - e^{-t/t_1})$ where A is a normalizing constant and (t_1, t_2) define the kinetics of the synapses: GABAergic conductance (t_1, t_2) = (0.5, 15) ms, AMPAR-dependent conductance (t_1, t_2) = (0.1, 1.8) ms, NMDAR-dependent conductance (t_1, t_2) = (0.5, 17.0) ms (ModelDB: https://senselab.med.yale.edu/ModelDB/). The magnesium block of NMDA receptors was modeled by a voltage-dependent factor [157]. Remaining free parameters comprised: the leaking conductivity g_m (or, equivalently, the membrane time constant T_m); the peak synaptic conductance per area: g_{AMPA}, g_{NMDA}, g_{GABA}; the total membrane area of the modeled neuron. These parameters were adjusted so that signal distributions fitted published electrophysiological recordings [110,113,116,158,159]. In more detail, we first set up one “ball-and-stick” model per segmented spine (N = 390). The dendrite hosting the modeled spine was generated as a tube of diameter $d_{dendrite}$ = 0.87 µm, and length $L_{dendrite}$ = 140 µm. This dendrite is split in three parts, the 2 µm-long middle one harboring the modeled spine. To account for the passive electrical effects of neighboring spines, the membrane surfaces of both the proximal and distal sections of the studied dendrite were scaled by a correction factor $\gamma = 1 + \langle A_{spine} \rangle d_{spine} / \pi d_{dendrite} = 3.34$, with the density d_{spine} = 1.63 spine.µm^{-1} and the average spine membrane area $\langle A_{spine} \rangle$ = 3.89 µm^2 . We calibrated synaptic conductances type by type, by fitting the signals generated in the whole distribution of 390 models to published electrophysiological recordings. The AMPA conductances of all excitatory synapses were set proportional to ePSD area and scaled by the free parameter g_A. In each model, we activated the AMPAR component of excitatory synapses and monitored the amplitude of resulting EPSCs in the soma. The average EPSC amplitude was adjusted to 58 pA [110,158], yielding a scaling factor g_A = 3.15 nS/µm^2, which takes into

account the average number of excitatory contacts per axon per PN in L2/3 of mouse SSC: $N_{ePSD/axon}$ = 2.8 [110]. The average AMPA synaptic conductance was 0.42 nS. The leakage resistance was fitted to 65 MΩ [114], yielding a total membrane surface of the modeled neurons: $A_{mb,total}$ = 18550 µm^2. The NMDA conductances of all excitatory synapses were set proportional to ePSD area and scaled by the free parameter g_N. In each model, we activated both NMDA and AMPA components of excitatory synapses and fitted the amplitude ratio between the average AMPA+NMDA and AMPA-only responses to 1.05 [158], yielding g_N = 3.4 nS/µm^2. The GABA conductances of all inhibitory synapses were set proportional to iPSD area and scaled by the free parameter g_G. In this case, we set the neuron to a holding potential of 0 mV and the reversal potential of chloride ions (E_{Cl}-) to -80 mV. Then, we activated shaft inhibitory synapses and monitored the amplitude of resulting IPSCs in the soma. The amplitude of the average GABAergic conductance was set to 1 nS [38,114,115], yielding a scaling factor g_G = 5.9 nS/µm^2, which takes into account the average number of inhibitory contacts per axon per PN in L2/3 of mouse SSC: $N_{iPSD/axon}$ = 6 [114]. Considering inhibition, since E_{Cl}- is regulated on timescales exceeding 100 ms [160] and we modeled signals in the 10 ms timescale, we could set E_{Cl}- as a constant parameter of our steady state model. Calcium influxes were modeled in spines as a result of the opening of NMDARs and voltage-dependent calcium channels (VDCCs). Since we simulated signals that remained below the threshold for eliciting dendritic spikes [35,74], we did not include VDCCs in dendrites, and monitored calcium transients exclusively in spine heads. The dynamics of L-, N- and Q-type VDCCs were obtained from ModelDB (accession n°: 151458), and their conductivities were scaled to the head membrane area of each spine, A_{head}, excluding synaptic area(s). VDCC-type ratios and calcium conductivities were adjusted by fitting the average amplitude of calcium concentration transients to 20% of the NMDA conductance [161]. Calcium uptake from cytosolic buffers was set to 95% to yield an average amplitude of Ca^{2+} concentration transients of 0.7 µM [162].

Bootstrapping

721 To simulate a large number of spine-spine interactions with limited redundancy, our
722 distribution of spines was expanded using a "smooth" bootstrapping method [121].
723 Specifically, the dataset (i.e. a matrix of dimensions N x N_f) was re-sampled to generate a
724 new matrix of dimension M x N_f, where N is the number of spines, N_f is the number of
725 selected features, and M is the final number of synthetic spines. M rows were randomly
726 selected in the original dataset and zero-centered, feature-dependent Gaussian noise was
727 added to each element of the matrix (excluding absolute quantities, e.g. number of PSDs or
728 presence of SA). To determine appropriate noise amplitude for each parameter, a synthetic
729 set of M=500 spines was generated from the original dataset, including Gaussian noise with
730 an arbitrary amplitude σ, on one selected parameter. This new feature distribution was
731 compared to the original distribution using a 2-sample Kolmogorov-Smirnov test (KS-test),
732 and this procedure was repeated 1000 times for each set value of σ. A conservative noise
733 level (σ = 10%) was sufficient to smear parameter distributions while the fraction of synthetic
734 sets that were statistically different from the original set ($p < 0.05$, KS-test) remained 0 over
735 1000 iterations. σ = 10% was valid for all relevant features, and we assumed that such a
736 small noise amplitude would minimally interfere with non-linear correlations in our dataset.
737 Synthetically generated spines were then used to simulate elementary synaptic signaling
738 using in-house python scripts. We also used bootstrapping to estimate standard deviations
739 in our simulations.
740
741 **Statistics**
742 No statistical methods were used to predetermine sample size. We used a one-way ANOVA
743 on our 4 datasets (S1 Table) to test that inter-neuron and inter-mice variability were small
744 enough to pool all datasets together (S2 Table). We used Kolmogorov-Smirnov test to
745 determine that all measured morphological parameters followed a log-normal distribution (S2
746 Table). We used Mann–Whitney U test for statistical analyses of morphological parameters,
747 except when comparing the probability for SiSs and DiSs to harbor SA, for which we used
748 Pearson's χ^2 test. All results in the text are mean ± SD. In Fig 6,Fig 7 and Fig 9, we plot

749 medians as solid lines, as they better describe where log-normal distributions peak. Shaded
750 areas represent 68% confidence intervals, which span approximately one standard deviation
751 on each side of the mean.
752
753 **ACKNOWLEDGEMENTS**
754 We thank members of the Triller and Charrier laboratories (IBENS, Paris, France), Vincent
755 Hakim and Boris Barbour for insightful discussions. This work was supported by INSERM,
756 the Agence Nationale de la Recherche (ANR-13-PDOC-0003 and ANR-17-ERC3-0009 to
757 C.C.), the European Research Council (ERC starting grant 803704 to C.C.), the Labex
758 Memolife (901/IBENS/LD09 to O.G.), the company NIKON France via the CIFRE program
759 (convention n° 2015/1049 to O.G.) and the European Union's Horizon 2020
760 Framework Programme for Research and Innovation under the Specific Grant Agreement
761 No. 785907 (Human Brain Project SGA2 to P.S.). We acknowledge the ImagoSeine imaging
762 facility (Jean-Marc Verbavatz and Rémi Leborgne, Jacques Monod Institute, Paris, France)
763 for SBEM availability, service and support. We thank Liesbeth Hekkings (ThermoFisher
764 Scientific) for technical support. We are grateful to the IBENS Imaging Facility (France
765 BioImaging, supported by ANR-10-INBS-04, ANR-10-LABX-54 MEMO LIFE, and ANR-11-
766 IDEX-000-02 PSL* Research University, ‘‘Investments for the future’’; NERF 2011-45; FRM
767 DGE 20111123023; and FRC Rotary International France).
768
769 **AUTHOR CONTRIBUTIONS**
770 O.G. developed the 3D-CLEM workflow, performed the experiments, segmented images and
771 analyzed data. P.S. coded the model and analyzed data. N.A. and M.F. carried out the *in*
772 *utero* electroporations. P.R. trained O.G. in EM and carried out part of the TEM imaging.
773 O.G., P.R., A.T. and C.C. designed the study. O.G., P.S. and C.C. interpreted the results,
774 prepared the figures, and wrote the manuscript. A.T. and C.C. provided funding.
775

COMPETING INTERESTS

The authors declare that no competing interests exist.

REFERENCES

1. Ramon y Cajal S. Regias y consejos sobre investigacion biologica. Madrid Imprenta de Fontanet. 1899.
2. Hersch SM, White EL. Quantification of synapses formed with apical dendrites of golgi-impregnated pyramidal cells: Variability in thalamocortical inputs, but consistency in the ratios of asymmetrical to symmetrical synapses. Neuroscience. 1981;6. doi:10.1016/0306-4522(81)90069-5
3. Yuste R, Bonhoeffer T. Genesis of dendritic spines: Insights from ultrastructural and imaging studies. Nat Rev Neurosci. 2004;5: 24–34. doi:10.1038/nrn1300
4. Arellano JI. Ultrastructure of dendritic spines: correlation between synaptic and spine morphologies. Front Neurosci. 2007;1: 131–143. doi:10.3389/neuro.01.1.1.010.2007
5. Harris KM, Weinberg RJ. Ultrastructure of Synapses in the Mammalian Brain. Cold Spring Harb Perspect Biol. 2012. doi:10.1101/cshperspect.a005587
6. Harris KM, Spacek J, Bell ME, Parker PH, Lindsey LF, Baden AD, et al. A resource from 3D electron microscopy of hippocampal neuropil for user training and tool development. Sci Data. 2015;2: 1–19. doi:10.1038/sdata.2015.46
7. Fifková E, Anderson CL. Stimulation-induced changes in dimensions of stalks of dendritic spines in the dentate molecular layer. Exp Neurol. 1981;74: 621–627. doi:10.1016/0014-4886(81)90197-7
8. Nusser Z, Cull-Candy S, Farrant M. Differences in Synaptic GABAA Receptor Number Underlie Variation in GABA Mini Amplitude. Neuron. 1997;19: 697–709. doi:10.1016/S0896-6273(00)80382-7
9. Matsuzaki M, Honkura N, Ellis-Davies GCR, Kasai H. Structural basis of long-term potentiation in single dendritic spines. Nature. 2004;429: 761–766. doi:10.1038/255243a0

804 10. Bourne JN, Harris KM. Coordination of size and number of excitatory and inhibitory
805 synapses results in a balanced. Hippocampus. 2011;21: 354–373.
806 doi:10.1002/hipo.20768.COORDINATION
807 11. Holderith N, Lorincz A, Katona G, Rózsa B, Kulik A, Watanabe M, et al. Release
808 probability of hippocampal glutamatergic terminals scales with the size of the active
809 zone. Nat Neurosci. 2012;15: 988–997. doi:10.1038/nn.3137
810 12. Bailey CH, Kandel ER, Harris KM. Structural components of synaptic plasticity and
811 memory consolidation. Cold Spring Harb Perspect Biol. 2015;7: 1–29.
812 doi:10.1101/cshperspect.a021758
813 13. Kennedy MJ, Hanus C. Architecture and Dynamics of the Neuronal Secretory
814 Network. Annu Rev Cell Dev Biol. 2019;35: 1–24. doi:10.1146/annurev-cellbio-
815 100818-125418
816 14. Korkotian E, Frotscher M, Segal M. Synaptopodin regulates spine plasticity: Mediation
817 by calcium stores. J Neurosci. 2014;34: 11641–11651.
818 doi:10.1523/JNEUROSCI.0381-14.2014
819 15. Kubota Y, van Rijnsoever C, Kondo S, Karube F, Kawaguchi Y. Neocortical Inhibitory
820 Terminals Innervate Dendritic Spines Targeted by Thalamocortical Afferents. J
821 Neurosci. 2007;27: 1139–1150. doi:10.1523/JNEUROSCI.3846-06.2007
822 16. Alvarez VA, Sabatini BL. Anatomical and Physiological Plasticity of Dendritic Spines.
823 Annu Rev Neurosci. 2007;30: 79–97. doi:10.1146/annurev.neuro.30.051606.094222
824 17. Tønnesen J, Katona G, Rózsa B, Nägerl UV. Spine neck plasticity regulates
825 compartmentalization of synapses. Nat Neurosci. 2014;17: 678–685.
826 doi:10.1038/nn.3682
827 18. Adrian M, Kusters R, Storm C, Hoogenraad CC, Kapitein LC. Probing the Interplay
828 between Dendritic Spine Morphology and Membrane-Bound Diffusion. Biophys J.
829 2017;113: 2261–2270. doi:10.1016/j.bpj.2017.06.048
830 19. Yasuda R. Biophysics of Biochemical Signaling in Dendritic Spines: Implications in
831 Synaptic Plasticity. Biophys J. 2017;113: 2152–2159. doi:10.1016/j.bpj.2017.07.029

832 20. Harnett MT, Makara JK, Spruston N, Kath WL, Magee JC. Synaptic amplification by
833 dendritic spines enhances input cooperativity. Nature. 2012;491: 599–602.
834 doi:10.1038/nature11554
835 21. Yuste R. Electrical Compartmentalization in Dendritic Spines. Annu Rev Neurosci.
836 2013;36: 429–449. doi:10.1146/annurev-neuro-062111-150455
837 22. Tønnesen J, Nägerl UV. Dendritic spines as tunable regulators of synaptic signals.
838 Front Psychiatry. 2016;7. doi:10.3389/fpsyt.2016.00101
839 23. Svoboda K, Tank DW, Denk W. Direct measurement of coupling between dendritic
840 spines and shafts. Science. 1996. pp. 716–719. doi:10.1126/science.272.5262.716
841 24. Takasaki K, Sabatini BL. Super-resolution 2-photon microscopy reveals that the
842 morphology of each dendritic spine correlates with diffusive but not synaptic
843 properties. Front Neuroanat. 2014;8: 1–7. doi:10.3389/fnana.2014.00029
844 25. Popovic MA, Carnevale N, Rozsa B, Zecevic D. Electrical behaviour of dendritic
845 spines as revealed by voltage imaging. Nat Commun. 2015.
846 doi:10.1038/ncomms9436
847 26. Honkura N, Matsuzaki M, Noguchi J, Ellis-Davies GCR, Kasai H. The Subspine
848 Organization of Actin Fibers Regulates the Structure and Plasticity of Dendritic
849 Spines. Neuron. 2008;57: 719–729. doi:10.1016/j.neuron.2008.01.013
850 27. Araya R, Vogels TP, Yuste R. Activity-dependent dendritic spine neck changes are
851 correlated with synaptic strength. PNAS. 2014;111. doi:10.1073/pnas.1321869111
852 28. Androuin A, Potier B, Nägerl UV, Cattaert D, Danglot L, Thierry M, et al. Evidence for
853 altered dendritic spine compartmentalization in Alzheimer's disease and functional
854 effects in a mouse model. Acta Neuropathol. 2018;135: 839–854.
855 doi:10.1007/s00401-018-1847-6
856 29. Forrest MP, Parnell E, Penzes P. Dendritic structural plasticity and neuropsychiatric
857 disease. Nat Rev Neurosci. 2018;19: 215–234. doi:10.1038/nrn.2018.16
858 30. Rajkovich KE, Loerwald KW, Hale CF, Hess CT, Gibson JR, Huber KM. Experience-
859 Dependent and Differential Regulation of Local and Long-Range Excitatory

Neocortical Circuits by Postsynaptic Mef2c. Neuron. 2017;93: 48–56. doi:10.1016/j.neuron.2016.11.022

31. Poirazi P, Papoutsi A. Illuminating dendritic function with computational models. Nat Rev Neurosci. 2020. doi:10.1038/s41583-020-0301-7

32. Almog M, Korngreen A. Is realistic neuronal modeling realistic? J Neurophysiol. 2016;116: 2180–2209. doi:10.1152/jn.00360.2016

33. Rall W. Cable properties of dendrites and effects of synaptic location. Excit Synaptic Mech. 1970; 175–187.

34. Hodgkin AL, Huxley AF. A quantitative description of membrane current and its application to conduction and excitation in nerve. J Physiol. 1952;117: 500–544. doi:10.1109/ICCCT2.2017.7972284

35. Stuart GJ, Spruston N. Dendritic integration: 60 years of progress. Nat Neurosci. 2015;18: 1713–1721. doi:10.1038/nn.4157

36. Segev I, Rall W. Computational Study of an Excitable Dendritic Spine. J Neurophysiol. 1988. Available: http://jn.physiology.org/

37. Gidon A, Segev I. Principles Governing the Operation of Synaptic Inhibition in Dendrites. Neuron. 2012;75: 330–341. doi:10.1016/j.neuron.2012.05.015

38. Doron M, Chindemi G, Muller E, Markram H, Segev I. Timed Synaptic Inhibition Shapes NMDA Spikes, Influencing Local Dendritic Processing and Global I/O Properties of Cortical Neurons. Cell Rep. 2017;21: 1550–1561. doi:10.1016/j.celrep.2017.10.035

39. Yuste R, Majewska A, Holthoff K. From form to function: Calcium compartmentalization in dendritic spines. Nat Neurosci. 2000;3: 653–659. doi:10.1038/76609

40. Gulledge AT, Carnevale NT, Stuart GJ. Electrical advantages of dendritic spines. PLoS One. 2012;7. doi:10.1371/journal.pone.0036007

41. Jadi MP, Behabadi BF, Poleg-Polsky A, Schiller J, Mel BW. An augmented two-layer model captures nonlinear analog spatial integration effects in pyramidal neuron

888 dendrites. Proc IEEE. 2014;102: 782–798. doi:10.1109/JPROC.2014.2312671
889 42. Schüz A, Palm G. Density of neurons and synapses in the cerebral cortex of the
890 mouse. J Comp Neurol. 1989;286: 442–455. doi:10.1002/cne.902860404
891 43. Herculano-Houzel S, Watson C, Paxinos G. Distribution of neurons in functional areas
892 of the mouse cerebral cortex reveals quantitatively different cortical zones. Front
893 Neuroanat. 2013;7: 1–14. doi:10.3389/fnana.2013.00035
894 44. Motta A, Berning M, Boergens KM, Staffler B, Beining M, Loomba S, et al. Dense
895 connectomic reconstruction in layer 4 of the somatosensory cortex. Science (80-).
896 2019;366. doi:10.1126/science.aay3134
897 45. Sanes JR, Zipursky SL. Synaptic Specificity, Recognition Molecules, and Assembly of
898 Neural Circuits. Cell. 2020;181: 536–556. doi:10.1016/j.cell.2020.04.008
899 46. Briggman KL, Denk W. Towards neural circuit reconstruction with volume electron
900 microscopy techniques. Curr Opin Neurobiol. 2006;16: 562–570.
901 doi:10.1016/j.conb.2006.08.010
902 47. Helmstaedter M. Cellular-resolution connectomics: Challenges of dense neural circuit
903 reconstruction. Nat Methods. 2013;10: 501–507. doi:10.1038/nmeth.2476
904 48. Kasthuri N, Hayworth KJ, Berger DR, Schalek RL, Conchello JA, Knowles-Barley S,
905 et al. Saturated Reconstruction of a Volume of Neocortex. Cell. 2015;162: 648–661.
906 doi:10.1016/j.cell.2015.06.054
907 49. Karimi A, Odenthal J, Drawitsch F, Boergens KM, Helmstaedter M. Cell-type specific
908 innervation of cortical pyramidal cells at their apical dendrites. Elife. 2020;9: 1–23.
909 doi:10.7554/eLife.46876
910 50. De Boer P, Hoogenboom JP, Giepmans BNG. Correlated light and electron
911 microscopy: Ultrastructure lights up! Nat Methods. 2015;12: 503–513.
912 doi:10.1038/nmeth.3400
913 51. Begemann I, Galic M. Correlative light electron microscopy: Connecting synaptic
914 structure and function. Front Synaptic Neurosci. 2016;8: 1–12.
915 doi:10.3389/fnsyn.2016.00028

916 52. Müller-Reichert T, Verkade P. Correlative Light and Electron Microscopy III. Methods
917 in Cell Biology. 2017.
918 53. Watanabe S, Punge A, Hollopeter G, Willig KI, Hobson RJ, Davis MW, et al. Protein
919 localization in electron micrographs using fluorescence nanoscopy. Nat Methods.
920 2011;8: 80–84. doi:10.1038/nmeth.1537
921 54. Russell MRG, Lerner TR, Burden JJ, Nkwe DO, Pelchen-Matthews A, Domart M-C, et
922 al. 3D correlative light and electron microscopy of cultured cells using serial blockface
923 scanning electron microscopy. J Cell Sci. 2017;130: 278–291. doi:10.1242/jcs.188433
924 55. Collman F, Buchanan J, Phend KD, Micheva KD, Weinberg RJ, Smith SJ. Mapping
925 Synapses by Conjugate Light-Electron Array Tomography. J Neurosci. 2015;35:
926 5792–5807. doi:10.1523/JNEUROSCI.4274-14.2015
927 56. Lees RM, Peddie CJ, Collinson LM, Ashby MC, Verkade P. Correlative two-photon
928 and serial block face scanning electron microscopy in neuronal tissue using 3D near-
929 infrared branding maps. Methods in Cell Biology. Elsevier Ltd; 2017.
930 doi:10.1016/bs.mcb.2017.03.007
931 57. Maclachlan C, Sahlender DA, Hayashi S, Molnár Z, Knott G. Block Face Scanning
932 Electron Microscopy of Fluorescently Labeled Axons Without Using Near Infra-Red
933 Branding. Front Neuroanat. 2018;12: 1–8. doi:10.3389/fnana.2018.00088
934 58. Katz Y, Menon V, Nicholson DA, Geinisman Y, Kath WL, Spruston N. Synapse
935 Distribution Suggests a Two-Stage Model of Dendritic Integration in CA1 Pyramidal
936 Neurons. Neuron. 2009;63: 171–177. doi:10.1016/j.neuron.2009.06.023
937 59. Bosch C, Martínez A, Masachs N, Teixeira CM, Fernaud I, Ulloa F, et al.
938 Corrigendum: FIB/SEM technology and high-throughput 3D reconstruction of dendritic
939 spines and synapses in GFP-labeled adult-generated neurons. Front Neuroanat.
940 2015. doi:10.3389/fnana.2016.00100
941 60. Globus A, Rosenzweig M, Bennett E, Diamond M. Effects of differential experience on
942 dendritic spine counts in rat cerebral cortex. Comp Physiol Psychol. 1973;82: 175–81.
943 61. Feldmeyer D. Excitatory neuronal connectivity in the barrel cortex. Front Neuroanat.

2012;6: 1–22. doi:10.3389/fnana.2012.00024

62. Bian WJ, Miao WY, He SJ, Qiu Z, Yu X. Coordinated Spine Pruning and Maturation Mediated by Inter-Spine Competition for Cadherin/Catenin Complexes. Cell. 2015;162: 808–822. doi:10.1016/j.cell.2015.07.018

63. Luckner M, Burgold S, Filser S, Scheungrab M, Niyaz Y, Hummel E, et al. Label-free 3D-CLEM Using Endogenous Tissue Landmarks. iScience. 2018;6: 92–101. doi:10.1016/j.isci.2018.07.012

64. Meißlitzer-Ruppitsch C, Röhrl C, Neumüller J, Pavelka M, Ellinger A. Photooxidation technology for correlated light and electron microscopy. J Microsc. 2009;235: 322–335. doi:10.1111/j.1365-2818.2009.03220.x

65. Bishop D, Nikić I, Brinkoetter M, Knecht S, Potz S, Kerschensteiner M, et al. Near-infrared branding efficiently correlates light and electron microscopy. Nat Methods. 2011;8: 568–572. doi:10.1038/nmeth.1622

66. Maco B, Holtmaat A, Cantoni M, Kreshuk A, Straehle CN, Hamprecht FA, et al. Correlative In Vivo 2 Photon and Focused Ion Beam Scanning Electron Microscopy of Cortical Neurons. PLoS One. 2013;8: 1–7. doi:10.1371/journal.pone.0057405

67. Cane M, Maco B, Knott G, Holtmaat A. The relationship between PSD-95 clustering and spine stability In Vivo. J Neurosci. 2014;34: 2075–2086. doi:10.1523/JNEUROSCI.3353-13.2014

68. Blazquez-Llorca L, Hummel E, Zimmerman H, Zou C, Burgold S, Rietdorf J, et al. Correlation of two-photon in vivo imaging and FIB/SEM microscopy. J Microsc. 2015;259: 129–136. doi:10.1007/978-3-319-95849-1_8

69. Karreman MA, Hyenne V, Schwab Y, Goetz JG. Intravital Correlative Microscopy: Imaging Life at the Nanoscale. Trends Cell Biol. 2016;26: 848–863. doi:10.1016/j.tcb.2016.07.003

70. Lübke J. Photoconversion of diaminobenzidine with different fluorescent neuronal markers into a light and electron microscopic dense reaction product. Microsc Res Tech. 1993;24: 2–14. doi:10.1002/jemt.1070240103

71. Grabenbauer M, Geerts WJC, Fernadez-Rodriguez J, Hoenger A, Koster AJ, Nilsson T. Correlative microscopy and electron tomography of GFP through photooxidation. Nat Methods. 2005;2: 857–862. doi:10.1016/j.parco.2017.06.003

72. Ballesteros-Yáñez I, Benavides-Piccione R, Elston GN, Yuste R, DeFelipe J. Density and morphology of dendritic spines in mouse neocortex. Neuroscience. 2006;138: 403–409. doi:10.1016/j.neuroscience.2005.11.038

73. Chen JL, Villa KL, Cha JW, So PTC, Kubota Y, Nedivi E. Clustered Dynamics of Inhibitory Synapses and Dendritic Spines in the Adult Neocortex. Neuron. 2012;74: 361–373. doi:10.1016/j.neuron.2012.02.030

74. Sarid L, Feldmeyer D, Gidon A, Sakmann B, Segev I. Contribution of intracolumnar layer 2/3-to-Layer 2/3 excitatory connections in shaping the response to whisker deflection in rat barrel cortex. Cereb Cortex. 2015;25: 849–858. doi:10.1093/cercor/bht268

75. Kubota Y, Kondo S, Nomura M, Hatada S, Yamaguchi N, Mohamed AA, et al. Functional effects of distinct innervation styles of pyramidal cells by fast spiking cortical interneurons. Elife. 2015;4: 1–27. doi:10.7554/eLife.07919

76. Knott GW, Holtmaat A, Wilbrecht L, Welker E, Svoboda K. Spine growth precedes synapse formation in the adult neocortex in vivo. Nat Neurosci. 2006;9: 1117–1124. doi:10.1038/nn1747

77. Noguchi J, Nagaoka A, Watanabe S, Ellis-Davies GCR, Kitamura K, Kano M, et al. *In vivo* two-photon uncaging of glutamate revealing the structure-function relationships of dendritic spines in the neocortex of adult mice. J Physiol. 2011;589: 2447–2457. doi:10.1113/jphysiol.2011.207100

78. Bell M, Bartol T, Sejnowski T, Rangamani P. Dendritic spine geometry and spine apparatus organization govern the spatiotemporal dynamics of calcium. J Gen Physiol. 2019;151: 1017–1034. doi:10.1085/jgp.201812261

79. Noguchi J, Matsuzaki M, Ellis-Davies GCR, Kasai H. Spine-neck geometry determines NMDA receptor-dependent Ca2+ signaling in dendrites. Neuron. 2005;46:

609–622. doi:10.1016/j.neuron.2005.03.015

80. Bourne JN, Harris KM. Balancing Structure and Function at Hippocampal Dendritic Spines. Annu Rev Neurosci. 2008;31: 47–67. doi:10.1146/annurev.neuro.31.060407.125646

81. Segal M, Korkotian E. Endoplasmic reticulum calcium stores in dendritic spines. Front Neuroanat. 2014;8: 1–7. doi:10.3389/fnana.2014.00064

82. Chirillo MA, Waters MS, Lindsey LF, Bourne JN, Harris KM. Local resources of polyribosomes and SER promote synapse enlargement and spine clustering after long-term potentiation in adult rat hippocampus. Sci Rep. 2019;9: 1–14. doi:10.1038/s41598-019-40520-x

83. Spacek J, Harris KM. Three-dimensional organization of smooth endoplasmic reticulum in hippocampal CA1 dendrites and dendritic spines of the immature and mature rat. J Neurosci. 1997;17: 190–203. doi:10.1523/jneurosci.17-01-00190.1997

84. Elbohouty M, Wilson MT, Voss LJ, Steyn-Ross DA, Hunt LA. In vitro electrical conductivity of seizing and non-seizing mouse brain slices at 10 kHz. Phys Med Biol. 2013;58.

85. Miceli S, Ness T V., Einevoll GT, Schubert D. Impedance Spectrum in Cortical Tissue: Implications for Propagation of LFP Signals on the Microscopic Level. Eneuro. 2017;4: ENEURO.0291-16.2016. doi:10.1523/eneuro.0291-16.2016

86. Harris KM, Stevens JK. Dendritic spines of CA1 pyramidal cells in the rat hippocampus: Serial electron microscopy with reference to their biophysical characteristics. J Neurosci. 1989;9: 2982–2997. doi:10.1523/jneurosci.09-08-02982.1989

87. Jayant K, Hirtz JJ, Plante IJ La, Tsai DM, De Boer WDAM, Semonche A, et al. Targeted intracellular voltage recordings from dendritic spines using quantum-dot-coated nanopipettes. Nat Nanotechnol. 2017. doi:10.1038/nnano.2016.268

88. Lagache T, Jayant K, Yuste R. Electrodiffusion models of synaptic potentials in dendritic spines. J Comput Neurosci. 2019;47: 77–89.

1028 89. Jones EG, Powell TP. Morphological variations in the dendritic spines of the
1029 neocortex. J Cell Sci. 1969;5: 509–29. Available:
1030 http://www.ncbi.nlm.nih.gov/pubmed/5362339
1031 90. Beaulieu C, Colonnier M. A Laminar Analysis of the Number of Round-Asymmetrical
1032 and Flat- Symmetrical Synapses on Spines , Dendritic Trunks , and Cell Bodies in
1033 Area 17 of the Cat. J Comp Neurol. 1985;189: 180–189.
1034 91. Dehay C, Douglas RJ, Martin KAC, Nelson C. Excitation by geniculocortical synapses
1035 is not “vetoed” at the level of dendritic spines in cat visual cortex. J Physiol. 1991;440:
1036 723–734.
1037 92. Fifková E, Eason H, Schaner P. Inhibitory contacts on dendritic spines of the dentate
1038 fascia. Brain Res. 1992;577: 331–336. doi:10.1016/0006-8993(92)90293-I
1039 93. Micheva KD, Beaulieu C. Anatomical substrate for experience-dependent plasticity of
1040 the rat barrel field cortex. PNAS. 1995;92: 11834–11838.
1041 94. Knott GW, Quairiaux C, Genoud C, Welker E. Formation of Dendritic Spines with
1042 GABAergic Synapses Induced by Whisker Stimulation in Adult Mice. Neuron.
1043 2002;34: 265–273. doi:10.1016/S0896-6273(02)00663-3
1044 95. van Versendaal D, Rajendran R, Saiepour HM, Klooster J, Smit-Rigter L, Sommeijer
1045 JP, et al. Elimination of Inhibitory Synapses Is a Major Component of Adult Ocular
1046 Dominance Plasticity. Neuron. 2012;74: 374–383. doi:10.1016/j.neuron.2012.03.015
1047 96. Tyagarajan SK, Fritschy JM. Gephyrin: A master regulator of neuronal function? Nat
1048 Rev Neurosci. 2014;15: 141–156. doi:10.1038/nrn3670
1049 97. Krueger-Burg D, Papadopoulos T, Brose N. Organizers of inhibitory synapses come
1050 of age. Curr Opin Neurobiol. 2017;45: 66–77. doi:10.1016/j.conb.2017.04.003
1051 98. Fossati M, Pizzarelli R, Schmidt ER, Kupferman J V., Stroebel D, Polleux F, et al.
1052 SRGAP2 and Its Human-Specific Paralog Co-Regulate the Development of Excitatory
1053 and Inhibitory Synapses. Neuron. 2016;91: 356–369.
1054 doi:10.1016/j.neuron.2016.06.013
1055 99. Iascone DM, Li Y, Sümbül U, Doron M, Chen H, Andreu V, et al. Whole-Neuron

Synaptic Mapping Reveals Spatially Precise Excitatory/Inhibitory Balance Limiting Dendritic and Somatic Spiking. Neuron. 2020; 1–13. doi:10.1016/j.neuron.2020.02.015

100. Gray EG. Axo-somatic and axo-dendritic synapses of the cerebral cortex. J Anat. 1959;93: 420–433.

101. Uchizono K. Characteristics of excitatory and inhibitory synapses in the central nervous system of the cat. Nature. 1965;207: 642–643.

102. Isaacson JS, Scanziani M. How inhibition shapes cortical activity. Neuron. 2011;72: 231–243. doi:10.1016/j.neuron.2011.09.027

103. Boivin JR, Nedivi E. Functional implications of inhibitory synapse placement on signal processing in pyramidal neuron dendrites. Curr Opin Neurobiol. 2018;51: 16–22. doi:10.1016/j.conb.2018.01.013

104. Villa KL, Berry KP, Subramanian J, Cha JW, Oh WC, Kwon HB, et al. Inhibitory Synapses Are Repeatedly Assembled and Removed at Persistent Sites In Vivo. Neuron. 2016;89: 756–769. doi:10.1016/j.neuron.2016.01.010

105. Rall W. Theoretical significance of dendritic trees for neuronal input-output relations. Neural Theory Model. 1964; 73–97.

106. Dayan P, Abbott LF. Theoretical Neuroscience : Computational and Mathematical Modeling ofNeural Systems. MIT Press. 2001.

107. Stuart G, Spruston N, Häusser M. Dendrites. Oxford University Press. 2016.

108. Nusser Z, Hájos N, Somogyi P, Mody I. Increased number of synaptic GABAA receptors underlies potentiation at hippocampal inhibitory synapses. Nature. 1998;395: 172–177.

109. Koch C, Segev I. The role of single neurons in information processing. Nat Neurosci. 2000;3: 1171–1177. doi:10.1038/81444

110. Feldmeyer D, Lübke J, Sakmann B. Efficacy and connectivity of intracolumnar pairs of layer 2/3 pyramidal cells in the barrel cortex of juvenile rats. J Physiol. 2006;575: 583–602. doi:10.1113/jphysiol.2006.105106

1084 111. Frick A, Feldmeyer D, Helmstaedter M, Sakmann B. Monosynaptic connections
1085 between pairs of L5A pyramidal neurons in columns of juvenile rat somatosensory
1086 cortex. Cereb Cortex. 2008;18: 397–406. doi:10.1093/cercor/bhm074
1087 112. Lefort S, Tomm C, Floyd Sarria JC, Petersen CCH. The Excitatory Neuronal Network
1088 of the C2 Barrel Column in Mouse Primary Somatosensory Cortex. Neuron. 2009;61:
1089 301–316. doi:10.1016/j.neuron.2008.12.020
1090 113. Scala F, Kobak D, Shan S, Bernaerts Y, Laturnus S, Cadwell CR, et al. Layer 4 of
1091 mouse neocortex differs in cell types and circuit organization between sensory areas.
1092 Nat Commun. 2019;10: 1–12. doi:10.1038/s41467-019-12058-z
1093 114. Hoffmann JHO, Meyer HS, Schmitt AC, Straehle J, Weitbrecht T, Sakmann B, et al.
1094 Synaptic conductance estimates of the connection between local inhibitor
1095 interneurons and pyramidal neurons in layer 2/3 of a cortical column. Cereb Cortex.
1096 2015;25: 4415–4429. doi:10.1093/cercor/bhv039
1097 115. Xu H, Jeong HY, Tremblay R, Rudy B. Neocortical Somatostatin-Expressing
1098 GABAergic Interneurons Disinhibit the Thalamorecipient Layer 4. Neuron. 2013;77:
1099 155–167. doi:10.1016/j.neuron.2012.11.004
1100 116. Kobayashi M, Hamada T, Kogo M, Yanagawa Y, Obata K, Kang Y. Developmental
1101 profile of GABAA-mediated synaptic transmission in pyramidal cells of the
1102 somatosensory cortex. Eur J Neurosci. 2008;28: 849–861. doi:10.1111/j.1460-
1103 9568.2008.06401.x
1104 117. Acker CD, Hoyos E, Loew LM. EPSPs Measured in Proximal Dendritic Spines of
1105 Cortical Pyramidal Neurons. eNeuro. 2016;3: 1–13. doi:10.1523/eneuro.0050-15.2016
1106 118. Pedregosa F, Varoquaux G, Gramfort A, Michel V, Thirion B, Grisel O, et al. Scikit-
1107 Learn: Machine Learning in Python. J Mach Learn Res. 2011;12: 2825–2830.
1108 119. Chiu CQ, Lur G, Morse TM, Carnevale NT, Ellis-Davies GCR, Higley MJ.
1109 Compartmentalization of GABAergic inhibition by dendritic spines. Science (80-).
1110 2013;340: 759–762. doi:10.1126/science.1234274
1111 120. Higley MJ. Localized GABAergic inhibition of dendritic Ca2+ signalling. Nat Rev

Neurosci. 2014;15: 567–572. doi:10.1038/nrn3803

121. Efron B, Tibshirani RJ. An Introduction to the Bootstrap. CRC Press. 1994.

122. Doyon N, Vinay L, Prescott SA, De Koninck Y. Chloride Regulation: A Dynamic Equilibrium Crucial for Synaptic Inhibition. Neuron. 2016;89: 1157–1172. doi:10.1016/j.neuron.2016.02.030

123. Hao J, Wang XD, Dan Y, Poo MM, Zhang XH. An arithmetic rule for spatial summation of excitatory and inhibitory inputs in pyramidal neurons. PNAS. 2009;106: 21906–21911. doi:10.1073/pnas.0912022106

124. Bono J, Wilmes KA, Clopath C. Modelling plasticity in dendrites: from single cells to networks. Curr Opin Neurobiol. 2017;46: 136–141. doi:10.1016/j.conb.2017.08.013

125. Chiu CQ, Barberis A, Higley MJ. Preserving the balance: diverse forms of long-term GABAergic synaptic plasticity. Nat Rev Neurosci. 2019;20: 272–281. doi:10.1038/s41583-019-0141-5

126. Koch C, Poggio T, Torre V. Nonlinear interactions in a dendritic tree: localization, timing, and role in information processing. PNAS. 1983;80: 2799–2802.

127. Gabernet L, Jadhav SP, Feldman DE, Carandini M, Scanziani M. Somatosensory integration controlled by dynamic thalamocortical feed-forward inhibition. Neuron. 2005;48: 315–327. doi:10.1016/j.neuron.2005.09.022

128. Berglund K, Schleich W, Wang H, Feng G, Hall WC, Kuner T, et al. Imaging synaptic inhibition throughout the brain via genetically targeted Clomeleon. Brain Cell Biol. 2008;36: 101–118. doi:10.1007/s11068-008-9031-x

129. Losonczy A, Makara JK, Magee JC. Compartmentalized dendritic plasticity and input feature storage in neurons. Nature. 2008;452: 436–441. doi:10.1038/nature06725

130. Sarid L, Bruno R, Sakmann B, Segev I, Feldmeyer D. Modeling a layer 4-to-layer 2/3 module of a single column in rat neocortex: Interweaving in vitro and in vivo experimental observations. Proc Natl Acad Sci. 2007;104: 16353–16358. doi:10.1073/pnas.0707853104

131. Almog M, Korngreen A. A quantitative description of dendritic conductances and its

application to dendritic excitation in layer 5 pyramidal neurons. J Neurosci. 2014;34: 182–196. doi:10.1523/JNEUROSCI.2896-13.2014

132. Müllner FE, Wierenga CJ, Bonhoeffer T. Precision of Inhibition: Dendritic Inhibition by Individual GABAergic Synapses on Hippocampal Pyramidal Cells Is Confined in Space and Time. Neuron. 2015;87: 576–589. doi:10.1016/j.neuron.2015.07.003

133. Markram H, Muller E, Ramaswamy S, Reimann MW, Abdellah M, Sanchez CA, et al. Reconstruction and Simulation of Neocortical Microcircuitry. Cell. 2015;163: 456–492. doi:10.1016/j.cell.2015.09.029

134. Rostaing P, Real E, Siksou L, Lechaire JP, Boudier T, Boeckers TM, et al. Analysis of synaptic ultrastructure without fixative using high-pressure freezing and tomography. Eur J Neurosci. 2006;24: 3463–3474. doi:10.1111/j.1460-9568.2006.05234.x

135. Korogod N, Petersen CCH, Knott GW. Ultrastructural analysis of adult mouse neocortex comparing aldehyde perfusion with cryo fixation. Elife. 2015;4: 1–17. doi:10.7554/eLife.05793

136. Kubota Y, Karube F, Nomura M, Kawaguchi Y. The Diversity of Cortical Inhibitory Synapses. Front Neural Circuits. 2016;10: 1–15. doi:10.3389/fncir.2016.00027

137. Tremblay R, Lee S, Rudy B. GABAergic Interneurons in the Neocortex: From Cellular Properties to Circuits. Neuron. 2016;91: 260–292. doi:10.1016/j.neuron.2016.06.033

138. Kuljis DA, Park E, Telmer CA, Lee J, Ackerman DS, Bruchez MP, et al. Fluorescence-based quantitative synapse analysis for cell-type specific connectomics. eNeuro. 2019. doi:10.1523/ENEURO.0193-19.2019

139. Nabavi S, Fox R, Proulx CD, Lin JY, Tsien RY, Malinow R. Engineering a memory with LTD and LTP. Nature. 2014;511: 348–352. doi:10.1038/nature13294

140. Hayashi-Takagi A, Yagishita S, Nakamura M, Shirai F, Wu YI, Loshbaugh AL, et al. Labelling and optical erasure of synaptic memory traces in the motor cortex. Nature. 2015;525: 333–338. doi:10.1038/nature15257

141. Segal M. Dendritic spines: Morphological building blocks of memory. Neurobiol Learn Mem. 2017;138: 3–9. doi:10.1016/j.nlm.2016.06.007

1168 142. Lisman J. A mechanism for the Hebb and the anti-Hebb processes underlying
1169 learning and memory. PNAS. 1989;86: 9574–9578. doi:10.1073/pnas.86.23.9574
1170 143. Feldman DE. The Spike-Timing Dependence of Plasticity. Neuron. 2012;75: 556–571.
1171 doi:10.1016/j.neuron.2012.08.001
1172 144. Graupner M, Brunel N. Calcium-based plasticity model explains sensitivity of synaptic
1173 changes to spike pattern, rate, and dendritic location. Proc Natl Acad Sci. 2012;109:
1174 3991–3996. doi:10.1073/pnas.1109359109
1175 145. Hayama T, Noguchi J, Watanabe S, Takahashi N, Hayashi-Takagi A, Ellis-Davies
1176 GCR, et al. GABA promotes the competitive selection of dendritic spines by
1177 controlling local Ca 2+ signaling. Nat Neurosci. 2013;16: 1409–1416.
1178 doi:10.1038/nn.3496
1179 146. Nakahata Y, Yasuda R. Plasticity of spine structure: Local signaling, translation and
1180 cytoskeletal reorganization. Front Synaptic Neurosci. 2018;10: 1–13.
1181 doi:10.3389/fnsyn.2018.00029
1182 147. Kimura F, Itami C, Ikezoe K, Tamura H, Fujita I, Yanagawa Y, et al. Fast activation of
1183 feedforward inhibitory neurons from thalamic input and its relevance to the regulation
1184 of spike sequences in the barrel cortex. J Physiol. 2010;588: 2769–2787.
1185 doi:10.1113/jphysiol.2010.188177
1186 148. Wehr M, Zador AM. Balanced inhibition underlies tuning and sharpens spike timing in
1187 auditory cortex. Lett to Nat. 2003;426: 442–446.
1188 149. Frenkel MY, Sawtell NB, Diogo ACM, Yoon B, Neve RL, Bear MF. Instructive Effect of
1189 Visual Experience in Mouse Visual Cortex. Neuron. 2006;51: 339–349.
1190 doi:10.1016/j.neuron.2006.06.026
1191 150. Bhatia A, Moza S, Bhalla US. Precise excitation-inhibition balance controls gain and
1192 timing in the hippocampus. Elife. 2019;8: 1–29. doi:10.7554/eLife.43415
1193 151. Fossati M, Assendorp N, Gemin O, Colasse S, Dingli F, Arras G, et al. Trans-Synaptic
1194 Signaling through the Glutamate Receptor Delta-1 Mediates Inhibitory Synapse
1195 Formation in Cortical Pyramidal Neurons. Neuron. 2019;104: 1081-1094.e7.

doi:10.1016/j.neuron.2019.09.027

152. Deerinck TJ, Bushong EA, Thor A, Ellisman MH. NCMIR Methods for 3D EM: A new protocol for preparation of biological specimens for serial block face scanning electron microscopy. Nat Cent Microsc Imag Res. 2010; 6.

153. Belevich I, Joensuu M, Kumar D, Vihinen H, Jokitalo E. Microscopy Image Browser: A Platform for Segmentation and Analysis of Multidimensional Datasets. PLoS Biol. 2016;14: 1–13. doi:10.1371/journal.pbio.1002340

154. Kremer JR, Mastronarde DN, McIntosh JR. Computer visualization of three-dimensional image data using IMOD. J Struct Biol. 1996;116: 71–76. doi:10.1006/jsbi.1996.0013

155. Hines ML, Carnevale NT. NEURON: A tool for neuroscientists. Neuroscientist. 2001;7: 123–135. doi:10.1177/107385840100700207

156. Barbour B. Analysis of Claims that the Brain Extracellular Impedance Is High and Non-resistive. Biophys J. 2017;113: 1636–1638. doi:10.1016/j.bpj.2017.05.054

157. Jahr CE, Stevens CF. A quantitative description of NMDA receptor-channel kinetic behavior. J Neurosci. 1990;10: 1830–1837. doi:10.1523/jneurosci.10-06-01830.1990

158. Hull C, Isaacson JS, Scanziani M. Postsynaptic Mechanisms Govern the Differential Excitation of Cortical Neurons by Thalamic Inputs. J Neurosci. 2009;29: 9127–9136. doi:10.1523/jneurosci.5971-08.2009

159. Avermann M, Tomm C, Mateo C, Gerstner W, Petersen CCH. Microcircuits of excitatory and inhibitory neurons in layer 2/3 of mouse barrel cortex. J Neurophysiol. 2012;107: 3116–3134. doi:10.1152/jn.00917.2011

160. Boffi JC, Knabbe J, Kaiser M, Kuner T. KCC2-dependent steady-state intracellular chloride concentration and ph in cortical layer 2/3 neurons of anesthetized and awake mice. Front Cell Neurosci. 2018;12: 1–14. doi:10.3389/fncel.2018.00007

161. Bloodgood BL, Giessel AJ, Sabatini BL. Biphasic Synaptic Ca Influx Arising from Compartmentalized Electrical Signals in Dendritic Spines. Stevens CF, editor. PLoS Biol. 2009;7: e1000190. doi:10.1371/journal.pbio.1000190

1224 162. Sabatini BL, Oertner TG, Svoboda K. The life cycle of Ca2+ ions in dendritic spines.
1225 Neuron. 2002;33: 439–452. doi:10.1016/S0896-6273(02)00573-1

1226

1227 **FIGURE LEGENDS**

1228 **Fig 1. CLEM imaging of identified spines within intact cortical circuits.**

1229 (A) Visualization of basal dendrites of a pyramidal neuron expressing cytosolic TdTomato in
1230 L2/3 of adult mouse SSC. DAB was photo-precipitated using focused UV light to insert
1231 correlative landmarks (pink dots in yellow circles).

1232 (B) Transmitted light image of the same field of view after DAB photo-precipitation. DAB
1233 precipitates are highlighted with yellow circles. Blood vessels are outlined with purple
1234 dashed lines.

1235 (C) Composite scanning EM (SEM) image displaying DAB patterning at the depth of the
1236 neuron of interest (yellow circles). Slight mismatch between LM and SEM observation planes
1237 resulted in DAB landmarks appearing in different z-planes during block-facing; the white line
1238 represents stitching between z-shifted images. In C1, landmarks are arranged as in B. C2 is
1239 a close-up on the soma of the electroporated neuron, labelled with three DAB landmarks
1240 (arrowheads). C3 corresponds to an orthogonal (x,z) view of the SEM stack along the green
1241 dashed line in C2. The superficial DAB layer enabled ROI targeting, and the deeper layer
1242 enabled retrospective identification of the target neuron.

1243 (D) 3D-reconstruction of dendrites of interest from the overview SEM stack. DAB landmarks
1244 are reconstructed in blue (in yellow circles). The red rectangle outlines the portion of dendrite
1245 represented in E and F.

1246 (E) Z-projection of the confocal stack corresponding to the portion of dendrite reconstructed
1247 in D. Letters identify individual spines.

1248 (F) 3D-EM reconstruction. Individual dendritic spines are manually segmented and randomly
1249 colored. Spines that were detected in EM but not in LM are labelled in red.

1250 Scale bars: A, B, C1, D: 10 µm; C2, C3: 5 µm; E, F: 2 µm.

1251

Fig 2. Spine morphometry along basal dendrites of layer 2/3 cortical pyramidal neurons.

(A) 3D-reconstruction of a dendritic spine from a SBEM stack. Dendritic shaft is in light green, spine neck in turquoise, spine head in blue and PSD surface in red. The following parameters were measured : PSD area, head diameter, neck diameter and neck length. Scale bar: 300 nm.

(B) Linear correlation of PSD area and spine head volume. R^2=0.82.

(C) Plot of the minimal spine neck diameter as a function of spine neck length. Spearman correlation coefficient is -0.58.

(D) Neck length as a function of spine head orientation, as quantified by the ratio of spine head diameter (D_{head}) over its length (L_{head}). $D_{head}/L_{head} < 1$ corresponds to a prolate spine head, which shape is stretched longitudinally with respect to the neck. $D_{head}/L_{head} > 1$ characterizes an oblate spine head, oriented orthogonally to the neck. The dashed line corresponds to $D_{head}/L_{head} = 1$. We did not observe any oblate spine with a long neck (non-existent spine morphology).

Fig 3. Ultrastructural comparison of spines with and without a spine apparatus.

(A) TEM images of spines either devoid of spine apparatus (SA-, left) or containing a spine apparatus (SA+, right, yellow arrowhead). Scale bars: 500nm.

(B) Proportion of SA- and SA+ spines. Histogram represents mean ± SD, from 390 spines in N=8 dendrites.

(C) Distribution of mean head diameter for SA- and SA+ spines. N=179 and 221, respectively ($p < 10^{-38}$).

(D) Distribution of ePSD area. ($p < 10^{-40}$)

(E) Distribution of mean neck diameter. ($p < 10^{-12}$)

(F) Probability of harboring a SA as a function of spine head volume. Blue: experimental data. Orange: sigmoid fit.

(G) Distribution of the diffusional resistance of the spine neck (W_{neck}) calculated based on

neck morphology. ($p < 10^{-5}$).

***$p < 0.001$ calculated using Mann-Whitney test.

Fig 4. Identification of excitatory and inhibitory synapse on DiSs using CLEM.

(A) Confocal image of basal dendrites of a cortical L2/3 PN that was electroporated with cytosolic TdTomato and GFP-GPHN to label inhibitory synapses. The magenta rectangle outlines the region enlarged in B.

(B) Enlargement of a portion of the dendrite in A harboring several dendritic spine (lettered). Spine “e” contains a cluster of GFP-GPHN (asterisk) and corresponds to a putative dually-innervated spine (DiS).

(C) 3D-EM reconstruction of the same dendritic fragment as in B. Dendritic shaft is colored in purple; individual spines and PSDs are colored randomly. Spines visible in EM but not in LM are labelled in red. The inhibitory PSD (colored in green) on spine “e” is identified based on the position of the GFP-GPHN cluster (asterisk in B and C). GFP-GPHN-negative PSDs are defined as excitatory.

(D) 3D-EM reconstruction of spine "e" (yellow) with its presynaptic partners (magenta and green). As the “green” axon also targets a neighboring dendritic shaft (blue), it is defined as inhibitory. Scale bars: A: 10 µm; B, C, D: 1 µm.

Fig 5. Anatomical properties of DiSs.

(A) Proportion of spines harboring 0, 1 or 2 synaptic contacts, quantified with CLEM. Histograms represent mean ± SD, from 390 spines in N=8 dendrites.

(B) Quantification of mean spine head diameter for SiSs (blue) and DiSs (red). ($p < 10^{-4}$).

(C) Proportion of SiSs and DiSs harboring a SA. ($p < 10^{-10}$ using Pearson’s χ^2 test)

(D-F) Quantification of neck length (D), the ratio between mean neck diameter and head volume (E) and the diffusional neck resistance (W_{neck}) (F) between SiSs and DiSs (solid lines, N=349 and 37, respectively) and between DiSs with SiSs of similar head volume (spines with $V_{head} > 0.05$ µm^3, dashed lines, N=186 and 34, respectively).

(G) Quantification of iPSD area in DiSs and dendritic shafts. N=37 and 62, respectively ($p < 10^{-6}$).

(H) Quantification of ePSD area in SiSs or DiSs. ($p < 10^{-5}$).

(I) Plot of iPSD area as a function of ePSD area in individual DiSs. The dashed line (y = x) highlights that the ePSD is larger than the iPSD in most of DiSs. N=37.

p-values were computed using Mann-Whitney test (B, D-H) or Pearson's χ^2 test (C). Only significant ($p < 0.05$) p-values are shown (*$p < 0.05$; **$p < 0.01$; ***$p < 0.001$).

Fig 6. Morphologically-constrained model of synaptic signaling.

(A) Schematic of the circuit model (A1) and representative time-course of excitatory (magenta) and inhibitory (green) conductance based on the kinetics of AMPA, NMDA and $GABA_A$ receptors (A2). All compartments include passive resistor-capacitor circuits to model cell membrane properties and optionally include an active conductance that models voltage-dependent currents (VDC). All modeled spines feature an excitatory synapse with glutamatergic AMPA and NMDA currents. Spines and dendritic compartments can also feature an inhibitory synapse with GABAergic currents. All conductances were scaled to PSD area (see Methods).

(B) Simulation of the time-courses of membrane depolarization following an EPSP, taking into account spine diversity (i.e. R_{neck}, ePSD area and distance to soma, as measured in CLEM). Membrane voltage is monitored over time in the spine head (blue), in the dendritic shaft in front of the spine (orange) and in the soma (green). Median voltage transients are plotted as solid lines. Shaded areas represent 68% confidence intervals, which span approximately one standard deviation on each side of the mean.

(C) Amplitude of evoked depolarization (ΔV_{max}) as a function of ePSD area at three distinct locations: head of SiSs (blue) or DiSs (magenta) where the EPSP was elicited, dendritic shaft 1 µm from the spine (orange) or soma (green).

(D) Attenuation of the amplitude of depolarization between the spine head and the dendrite as a function of the resistance of the neck (R_{neck}). The attenuation was calculated as: $\alpha = 1 - \Delta V_{max,\ shaft} / \Delta V_{max,\ spine}$. Red cross: mean value of α.

(E) Estimated amplitude of intracellular calcium concentration transients $\Delta[Ca^{2+}]_{max}$, following activation of NMDA receptors and VDCCs as a function of ePSD area. Three spiking outliers are not represented.

Fig 7. Effect of the distance between excitatory and inhibitory synapses on the integration of coincident EPSPs and IPSPs.

(A) Sketch: an EPSP was elicited in the spine and an IPSP in the shaft at a distance Δx from the spine.

(B-C) Voltage inhibition, inh_V, calculated in the soma (B) or in the spine head (C) as a function of Δx, for N=3700 iterations of the model. On-path inhibition: $\Delta x > 0$; off-path inhibition: $\Delta x < 0$. Solid lines represent medians. Shaded areas represent 68% confidence intervals, which span approximately one standard deviation on each side of the mean.

Fig 8. Effect of dendritic and spinous inhibition on EPSPs.

(A) Sketches: an EPSP (arrow) was elicited in a bootstrapped DiS placed randomly along the dendrite, and an IPSP (⊤ symbol) was elicited either in the dendritic shaft at $\Delta x = 0.7$ µm from the stem of the spine (A1, blue) or directly in the spine head (A2, orange).

(B-C) Quantification of the inhibitory impact, inh_V, in the soma (B) and in the spine head (C) for N=3700 iterations of the model. Blue: dendritic inhibition; Orange: spinous inhibition.

Fig 9. Effect of input timing on EPSP and IPSP integration.

(A) Schematic: excitatory AMPA and NMDA conductances were activated at t=0. The inhibitory GABAergic conductance was activated at an interval Δt before or after the onset of excitation.

(B) Examples of the time-course of depolarization in the spine head for Δt = +5 ms (B1) and Δt = -5 ms (B2) (purple curves) compared to no inhibition (magenta curves) for E_{Cl^-} = -80 mV and V_{rest} = -70 mV. Arrows represent the onset of excitatory and inhibitory inputs (magenta and green arrows, respectively). τ_E represents the 80-to-20% decay time (case with no inhibition).

(C) Ratio of 80-to-20% decay time of membrane depolarizations in the presence of inhibition (τ_{E+I}) over that without inhibition (τ_E) as a function of Δt for dendritic (blue) or spinous (orange) inhibition. Solid lines represent medians. Shaded areas represent 68% confidence intervals, which span approximately one standard deviation on each side of the mean.

(D) Voltage inhibition in the spine head, inh_V, induced by dendritic (blue) or spinous (orange) IPSPs as a function of Δt.

(E) Inhibition of the calcium influx in the spine head, $inh_{[Ca2+]}$, induced by dendritic (blue) or spinous (orange) IPSPs as a function of Δt.

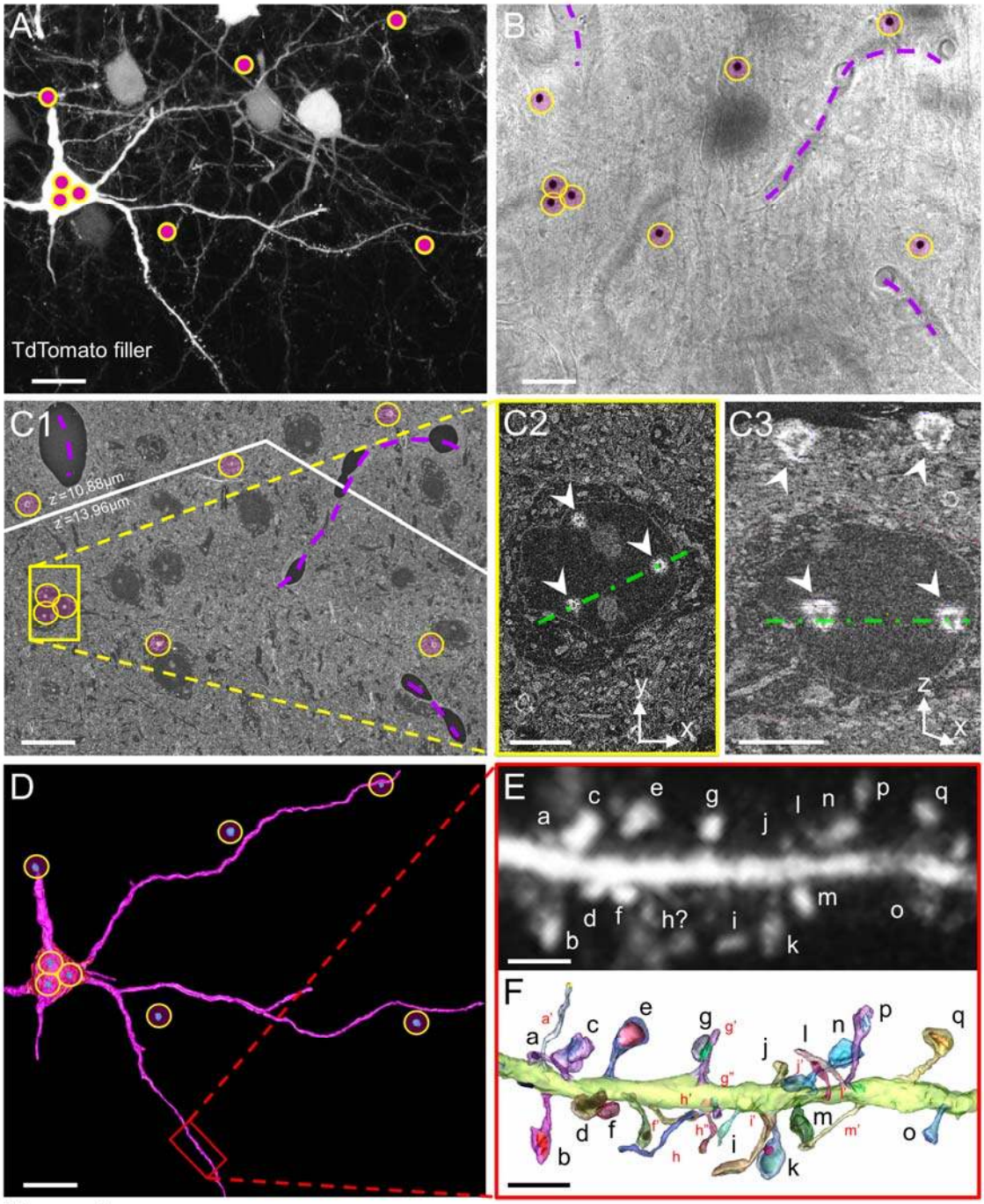

Figure 1

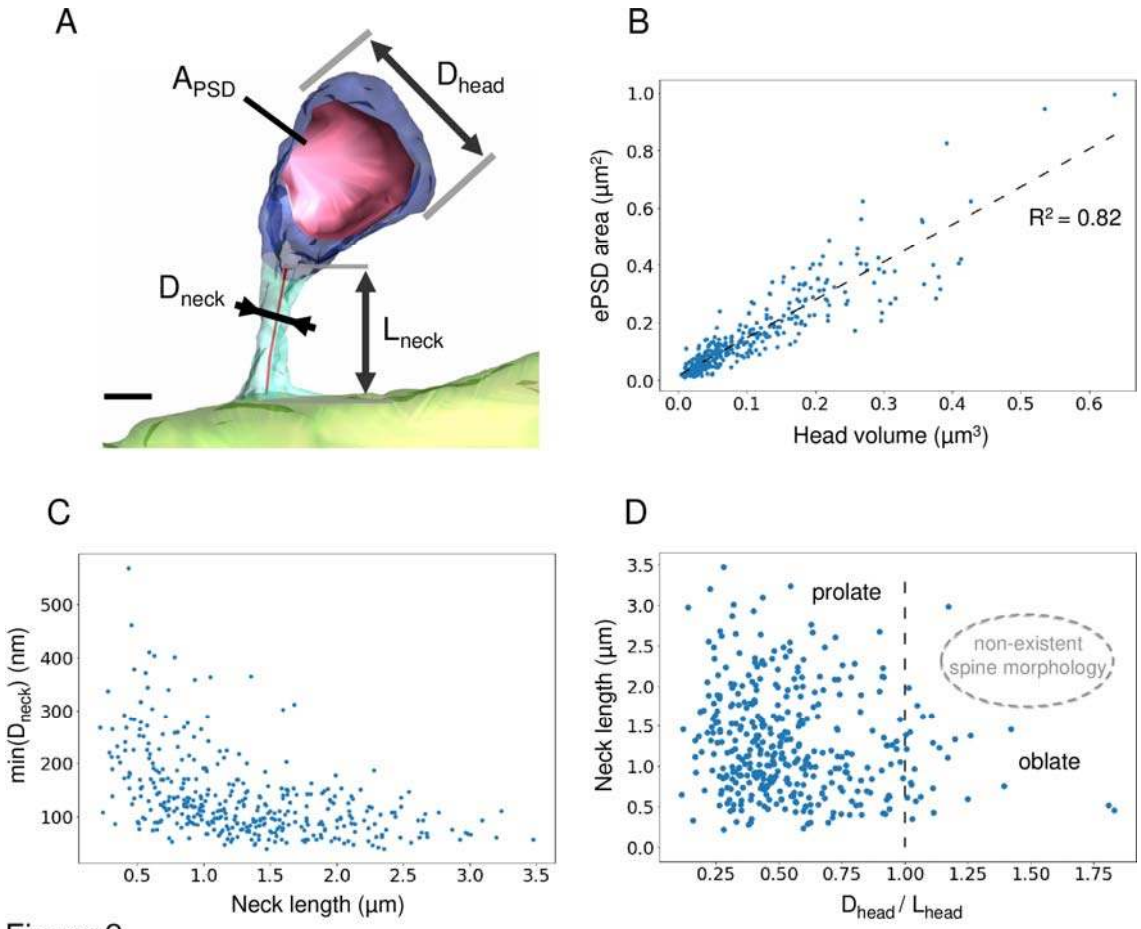

Figure 2

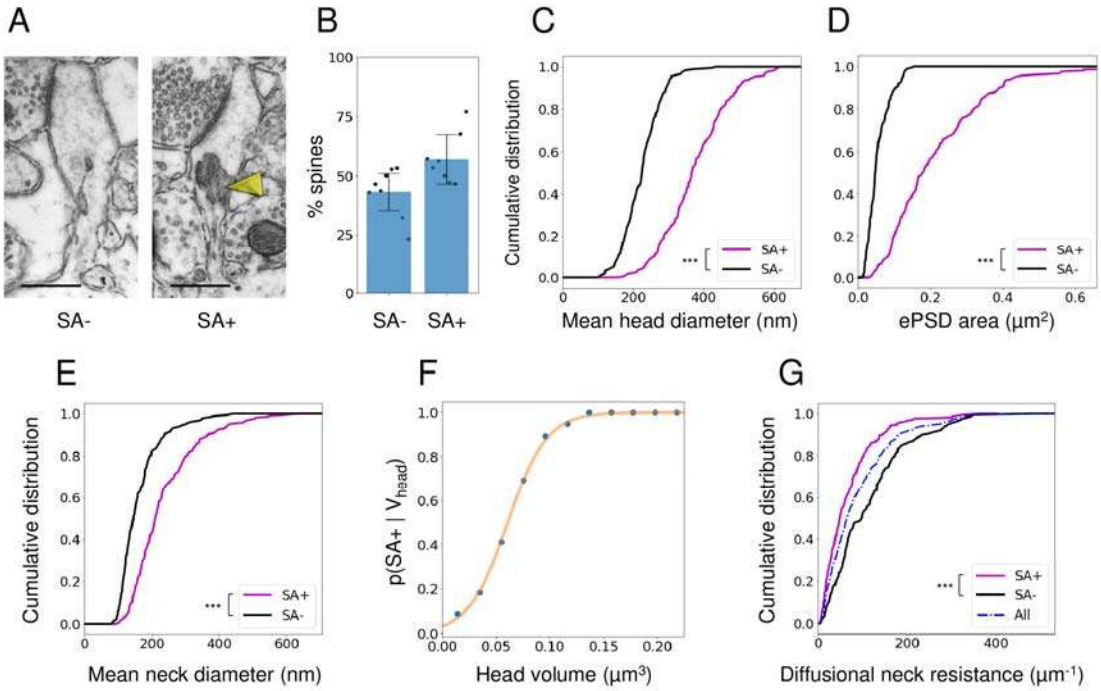

Figure 3

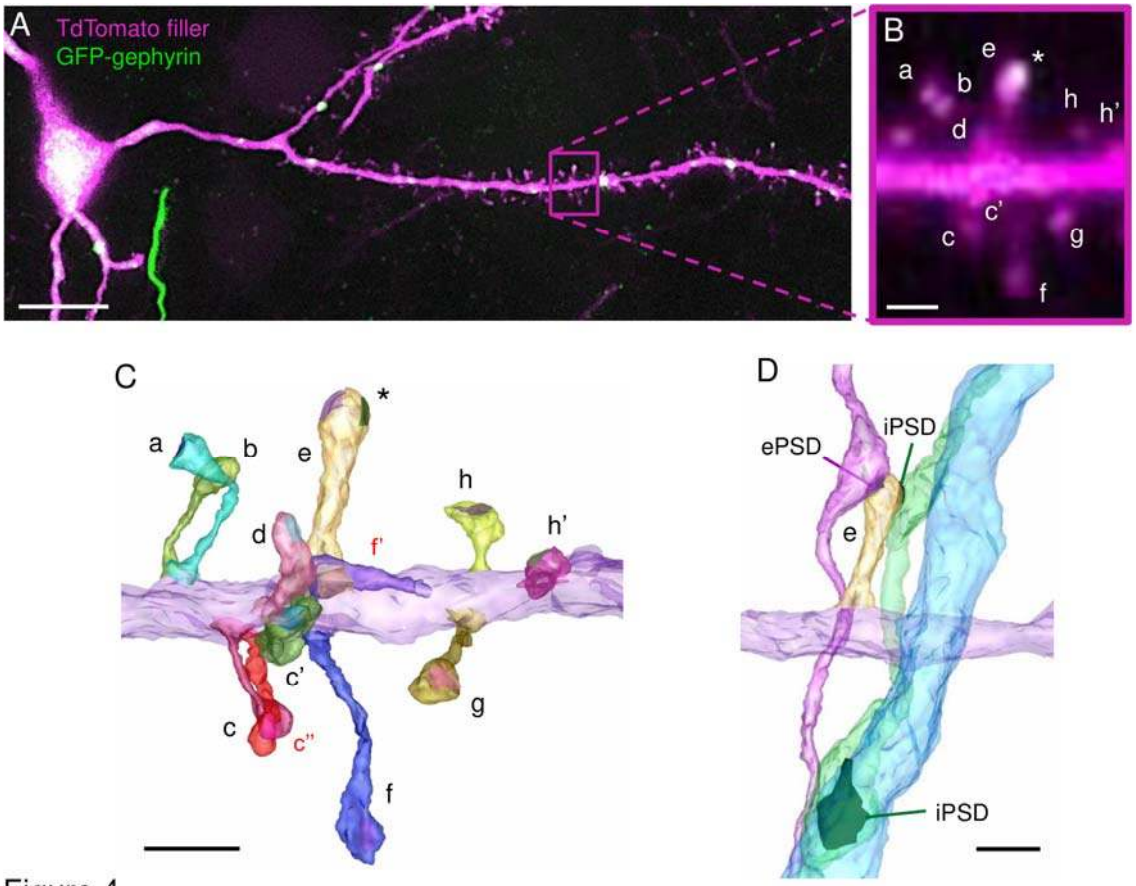

Figure 4

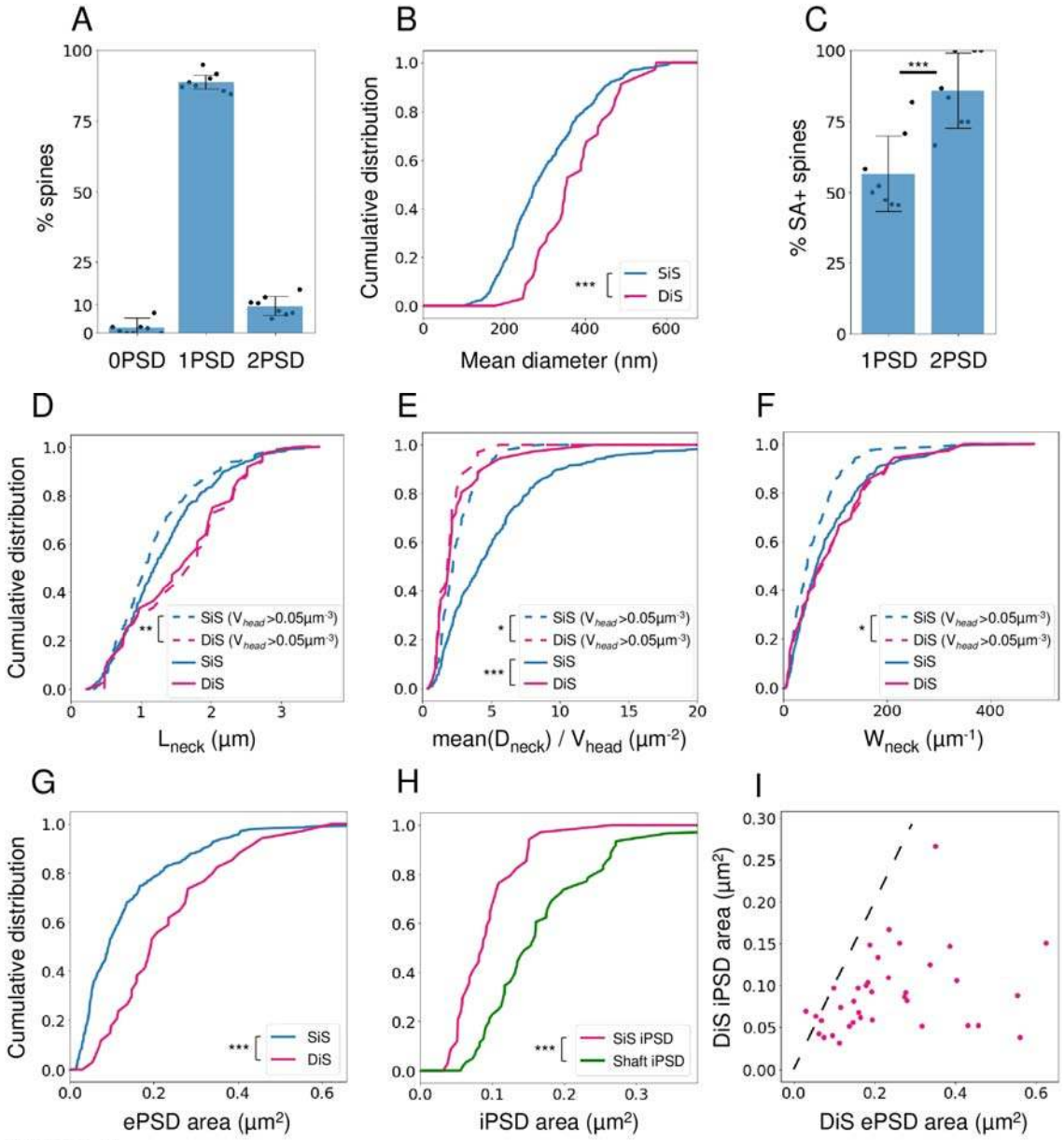

Figure 5

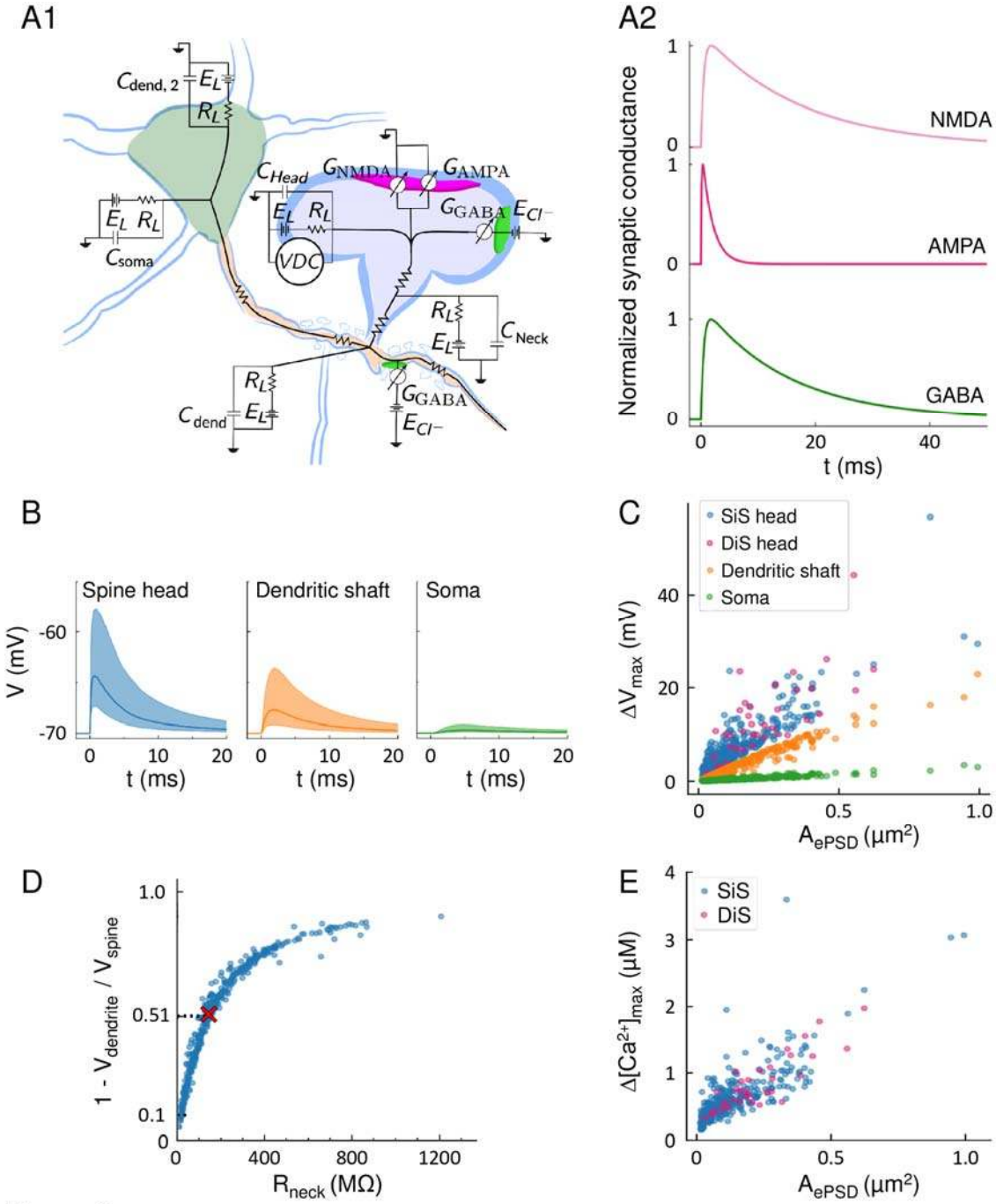

Figure 6

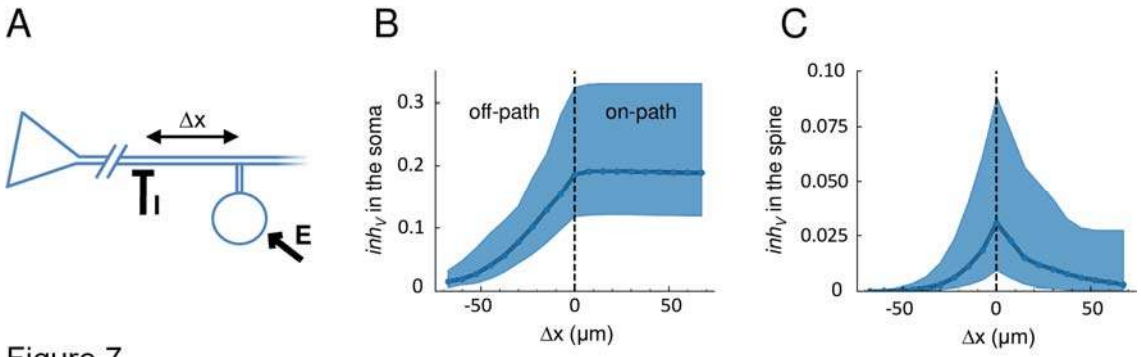

Figure 7

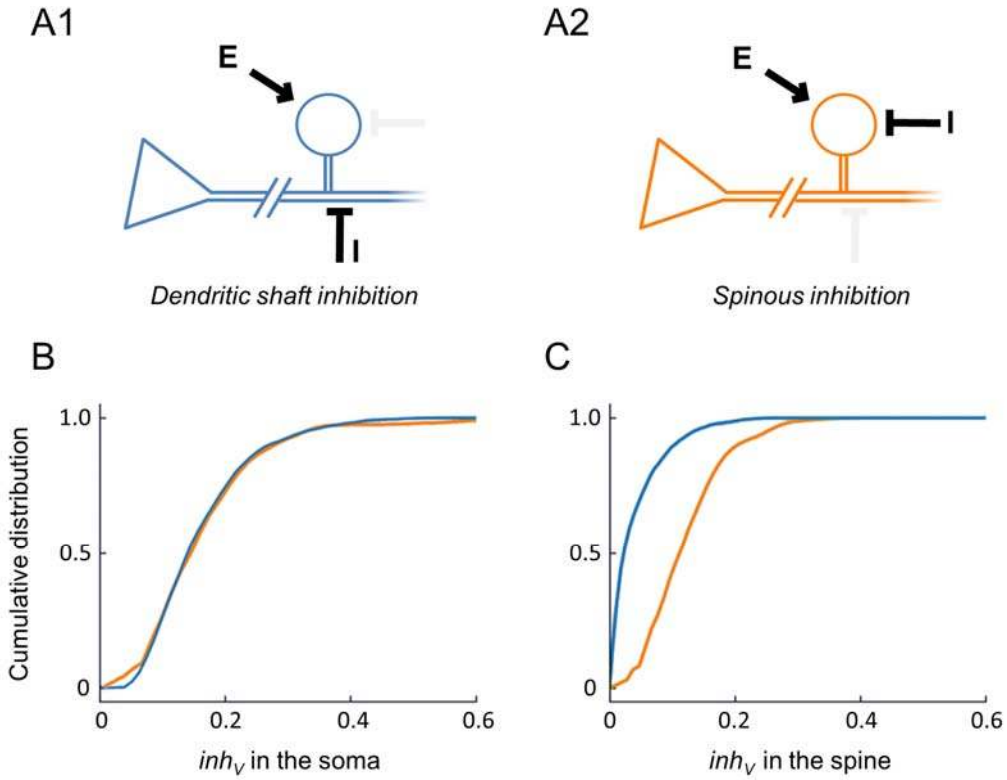

Figure 8

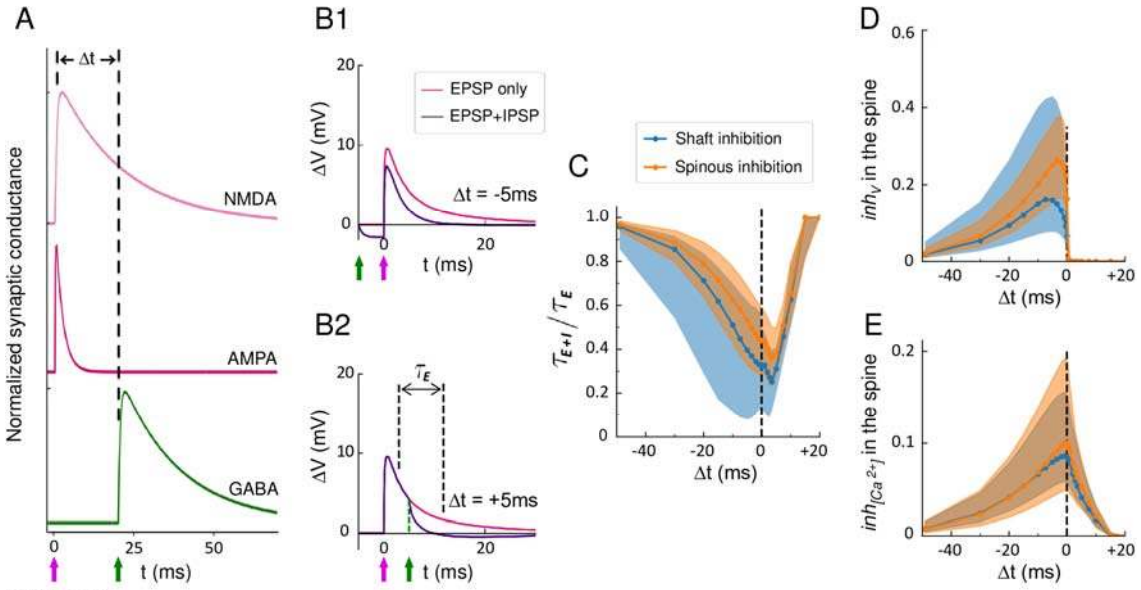

Figure 9